Politecnico di Torino

Master of Science in Automotive Engineering
A.Y. 2022/2023
Graduation Session December 2023

Analysis of the metamaterials for NVH vehicle applications

Rapporteurs:

    Luigi Garibaldi
    Alessandro Daga

Candidate:

    David Agabiti   s286347

Index

1. Introduction

The study of noise vibration and harshness plays an important role in vehicles since it permits to improve passenger safety and comfort.
Effects such as fatigue, annoyance, lower attention, missed alarms, vision and acoustic stress are addressed and reduced, thus lowering the risks when driving [1].
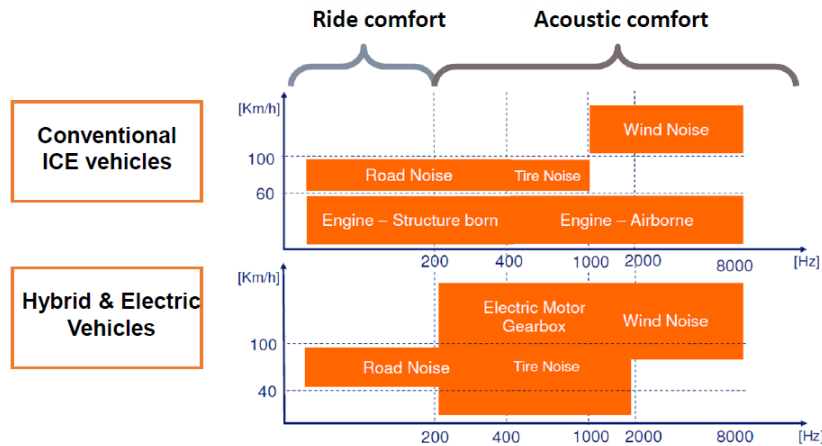
Figure 1: different type of noise as a function of speed and frequency for ICE and Hybrid and electric vehicles [2].

Other than that, for traditional ICE vehicles lightweight design solutions are increasingly in demand for both for emission reductions purposes and other several factors such as fuel efficiency, mileage life of tires and vehicle performances [3]. It should be also considered that with the passage from conventional ICE vehicles to hybrid and electric vehicles some of the excited frequency ranges and source of noise changed will change too, as shown in figure 1.

In order to address all these issues, one of the most recent solutions in the NVH field is the use of metamaterials that not only allow to decrease noise and vibration but can also reduce the weight on the vehicle.
These materials are engineered in order to have properties that are not found in naturally occurring materials, properties that can be controlled by designing their macro units.
They are obtained from the periodical disposition of a unit cell, which is composed of a host structure, usually a metal surface, and a local resonator which is the principal subject of study.
The metamaterials are characterized by a frequency region called stopband, in which the transmission of elastic waves is inhibited, and so, noise and vibration reduction is expected.
The bandgap can be obtained by two mechanisms, that is local resonance and Bragg scattering.
The former "attenuates elastic waves with a wavelength comparable to the length of the unit cell, and so if we want to work in frequency ranges under 1 kHz with Bragg scattering, using a unit cell with an extremely low specific stiffness or using an unrealistically large unit cell is required" [4].
For this reason, in automotive field it is more suitable the local resonance mechanism "that have been shown to attenuate waves with wavelengths two orders of magnitude greater than the lattice constant of the metamaterial" [5]. This former aspect makes metamaterials particularly well suited for low frequency applications, especially if we consider that conventional NVH solutions require heavy and bulky systems for these frequency ranges.

The bandgap is so obtained from the out of phase vibration from the local resonators that interferes with the sound or vibration wave that is propagating in the material with a frequency similar to the one of the local resonances of the resonator [6].

In addition, the stopband can also be tuned by varying the geometric characteristics of the resonant structure, a fact that permits to reach an even wider frequency region in which NVH is attenuated. This, for example is exploited in plates with multiple periodic distribution of the same concept of resonator but with different geometry.
As said before, their capability to achieve both low frequency bandgap along with a compact and lightweight design makes them well suited for automotive applications.

1.1 Nomenclature

Symbol	Definition	Measurement unit
K	stiffness matrix	
C	damping matrix	
M	mass matrix	
q	generalised displacement	
F	generalised force	
u	complex deflection	m
t	time	s
k, μ	wave vector	rad/m
k_x	wave vector component along the x axis	rad/m
k_y	wave vector component along the y axis	rad/m
x	position	m
r	position vector	m
IBC	Irreducible Brillouin Contour	
UC	unit cell	
τ_c	torsional stiffness	Nm/rad
l	depth	mm
h, b	height	mm
w	width	mm
d	diameter	mm
FRF	frequency response function	
BWa	bandgap-midgap ratio	
BG	bandgap	Hz
SCFRPs	short carbon fiber-reinforced plastics	
CCFRPs	continuous carbon fiber-reinforced plastics	
BS	Bragg Scattering phenomenon	
α	absorption coefficient of the metamaterial panel	
LRM	local resonant metamaterial	

STL	sound transmission loss	dB
f	frequency	Hz
ρ_{host}	bare host structure mass density	kg/m^3
1.8 ρ_{host}	equivalent static mass density	kg/m^3
FEM	finite element method	
D	driver position sensor	
FP	front passenger position sensor	
RP	rear passenger position sensor	
ΔSPL	difference between the bare configuration SPL and the metamaterial solution SPL	dBA/Hz
MSV	mean square velocity	m^2/s^2
RSP	radiation sound power	W
s, a	metamaterial periodicity in a given direction	m
BC	boundary condition	
ii	arbitrary user defined parameter	

1.2 Unit cell nomenclature
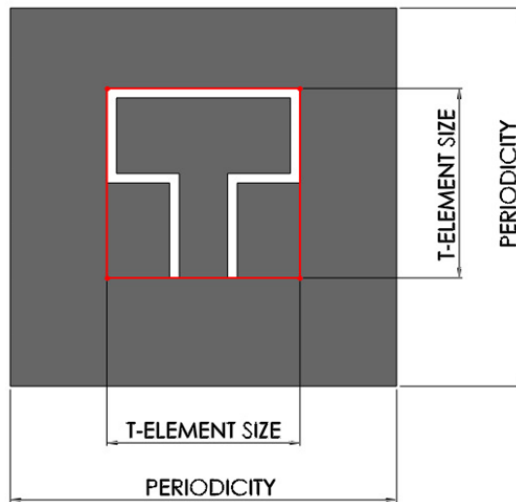
Figure 2: unit cell example.

Let us now define some of the terms for the unit cell geometry. As it can be seen from the image above, the periodicity is the unit cell dimension along a given axis and it is used in reference to all the proposed metamaterial solutions.

The T-element size, instead, is the length of the square (represented in red in figure 2) in which the T shaped part of the application [7] is inscribed. This term will be mainly utilized for the topology optimization phase.

2. Metamaterial property analysis

Generally, the standard procedure followed for testing these materials is composed, at the beginning, by a unit cell FEM analysis in order to obtain the dispersion curves and evaluate the bandgap. A subsequent finite plate FEM analysis is performed, followed by one or more lab tests in which the material is built and validated experimentally.

For what concern the unit cell modelling, under the hypothesis of infinitely periodically arranged metamaterial along the x and y direction, a single unit cell is considered. It is represented by a finite element model whose equation of motion for a harmonic excitation are described as:

$$(K + j\omega C - \omega^2 M)\, q = F, \quad (1)$$

In which, K is the stiffness matrix, C is the damping matrix (which in most of the cases proposed is considered equal to 0), M is the mass matrix, q and F are the generalised displacement and force and ω is the frequency.

"Let us now consider the 1D elastic wave propagation equation:

$$u(x,t) = u_0 * e^{i(kx-\omega t)} \quad (2)$$

where u stands for complex deflection, x stands for position, t stands for time, k is the wave number, ω is the angular frequency and u_0 is the amplitude. If we consider only the wave propagation in space (x axis), which is given by the kx term, $u(x)$ can be calculated at every position on the x axis when the wave number is known. Considering a 1D periodic grid with a unit cell spacing of the length a, we would be able to link the amplitude from the starting of the unit cell (x_0) to the end ($x_1 = x_0 + a$) in the form:

$$u(x_1) = u(x_0) * e^{ika} \quad (3)$$

This is called Bloch theorem [8] and can be expressed more generally for 3D elastic waves as:

$$u(r_1) = u(r_0) * e^{ik(r_1-r_0)} \quad (4)$$

with u as deflection vector, k as wave vector that describes the propagation direction of the elastic wave and r_0 and r_1 as the position vectors at the beginning and at the end of the unit cell. This expression can be used to define boundary conditions for a unit cell" [9]. As a consequence, the unknown quantities in the equations of motion for the unit cell (1) are reduced in number, as demonstrated in [10].

By doing so, it is obtained an eigenvalue problem such as:

$$A\big(\omega, k_x, k_y\big) q^{(red)} = 0 \quad (5)$$

In which A is a general matrix, which is function of the frequency ω and the wave number components k_x and k_y, while $q^{(red)}$ is a reduced set of generalized displacements. From the solution of the matrix A the dispersion curves are obtained.

"Classically, Eq. (5) is solved as a linear EVP using an inverse approach, assuming free wave propagation, thus imposing a set of real k = (k$_x$, k$_y$), solving for real ω along the Irreducible Brillouin Contour" [11].

A bandgap is precisely identified when no free wave solution is found, and so, in this frequency region a noise and vibration attenuation is expected.

2.1 Dispersion diagram description

The elastic waves that propagate in a waveguide can be considered as the sum of wave modes that are characterized by their own wavelength and frequency. "These wave modes are specific of each structure and can be represented by mean of the dispersion curves. [...] It is worth mentioning that the dispersion curves are a tool to understand the wave propagation in the studied geometry. These curves are like a map that contains all the possible wave modes that can be propagated in a specific guided wave for each combination of frequency and wave number" [12].

From these curves, in practice, we can understand what is the allowed frequency band and what is the forbidden band for a given wave mode.
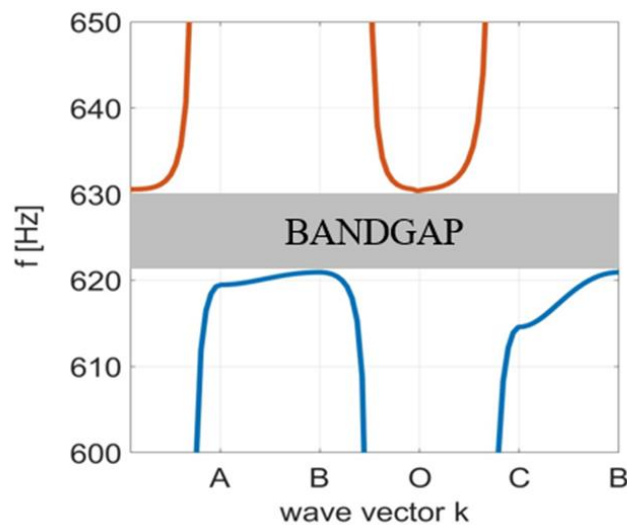
Figure 3: dispersion diagram example

A frequency range in which no free wave solution is found among all the modes, is called bandgap or stopband, as represented in the diagram above, too. It is defined as complete if the forbidden band takes place for all the directions of the Irreducible Brillouin Contour, otherwise, it will be defined as partial. As said before, in the stopband a noise and vibration attenuation is expected.

Below are reported a set of metamaterial applications, subdivided in vibration attenuation and sound attenuation category.

3. Vibration attenuation applications

Mechanical resonators

3.1 Torsional local resonators metamaterial

The proposed metamaterial unit cell consists in a torsional local resonator periodically arranged on a beam. For what concern the analytical approach, it was utilised both the Timoshenko beam theory and Bloch's theorem in order to evaluate the dispersion relation.

For the numerical model approach, instead, the BEAM188 property has been assigned to the host beam and the resonant structure is described with the combination of the structural mass element MASS21 and one-dimensional two-node spring element COMBIN14.

By performing a unit cell analysis, a stopband region is noted in the 86.8Hz ~ 89.5Hz range, as shown in figure 4. "Besides, it is found that with the increase of the torsional stiffness τ_c, the band gap is widened and moves to a higher frequency" [6].

Then, it was performed a FEM analysis for a finitely long model with different torsional local resonators.
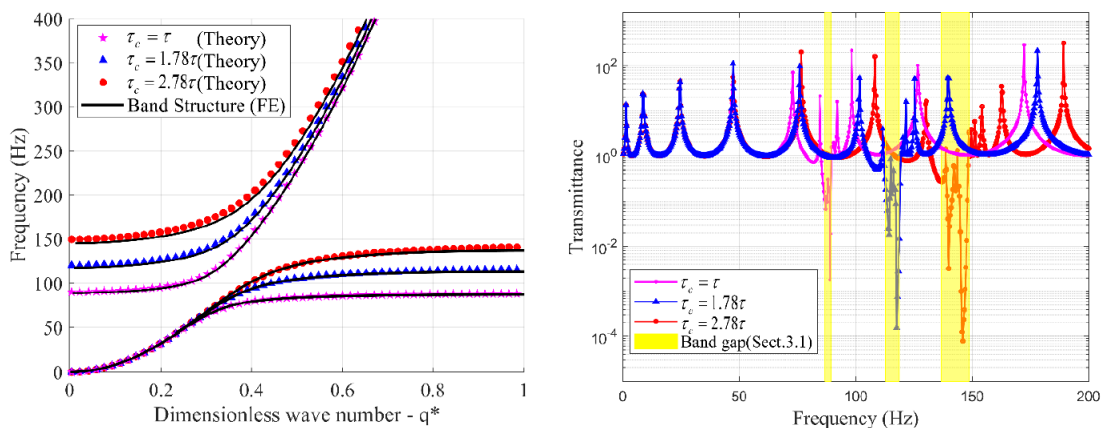
Figure 4 (left): comparison of band structure predicted based on theory and FE simulation with different torsional stiffnesses τc; (right): transmittances of metamaterial beam with different torsional stiffnesses τ_c.

From the obtained results in figure 4, they are notable three different regions in which the transmittance is strongly reduced, corresponding to the bandgaps of the three types of local resonators. It is also worth to notice that the stopband begins before the local resonant frequency and its upper bound corresponds to the torsional resonator local resonant frequency [6].

3.2 Square Z-shaped frame local resonator metamaterial

The proposed metamaterial unit cell is composed of a thin homogenous plate host structure and a local resonator which consists of a square z-shaped frame, two trapezoidal plates and a M4 screw, as shown in figure 5.
The frame material is aluminium, while the trapezoidal plates are in structural steel and aluminium.
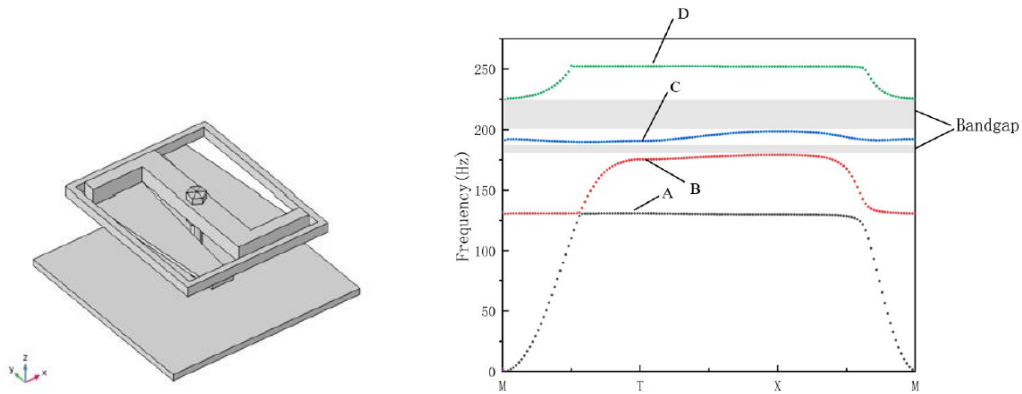
Figure 5 (left): configuration of the metamaterial unit cell, (right): Band structures of the metamaterial aluminium plate with periodic resonator.

Exploiting the methodology in paragraph 2, a unit cell analysis is numerically simulated in order to evaluate the band structure. From the obtained results shown in figure 5, two complete bandgaps are present in the 178-198 Hz and 198-225 Hz respectively.

Then, a full plate is simulated with a sinusoidal excitation in its center at 185 Hz and 210 Hz, that are two frequencies inside the stop band region.
The results confirm the expectations, and from the comparison of the untreated and treated case, a major modal displacement reduction and vibration attenuation are achieved in the considered bandgap region [13].
Basing on its two bandgaps and performances, the proposed metamaterial cold be a promising application in NVH automotive field, but it may be limited by the fact that its particular shape could be more expensive than others to produce in large scale and so these could be preferred with respect to it.

3.3 T-shaped local resonator metamaterial

The presented metamaterial unit cell has a structure composed by a narrow beam bent upwards with a wide final section that is bent in its turn in order to achieve a more compact package and a simpler fabrication procedure. The presented shape is achieved by a punching and a bending process over some aluminium alloy EN AW-6082 samples.

Under the hypothesis of an infinite periodic system and low damping, a single cell inverse modelling approach was implemented for the FEM band structure analysis. The results reported in figure 6, indicate that a stop band is found between 615 Hz and 635 Hz.
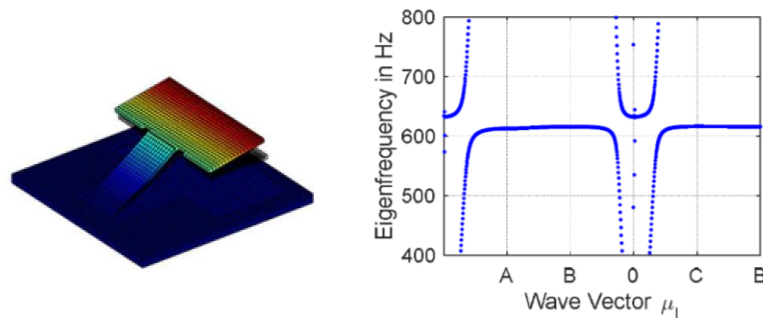
Figure 6: Resonator concept in its first eigenmode (left), dispersion relation (right).

Then, a full plate structure is modelled and simulated. The mass increase due to the local resonator addition is about 20% with respect to the host structure.
The obtained results show that the stop band is shifted towards the 580 – 610 Hz frequency range which is in lower values with respect to the expected ones.
After that, the full plate was experimentally validated and the mean FRF was evaluated.
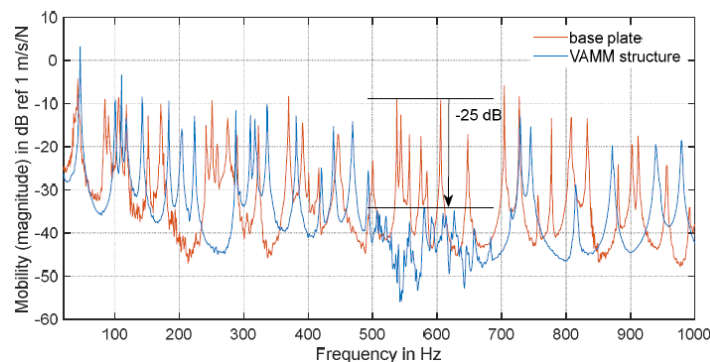
Figure 7: plate experimental test results (right).

From the obtained diagram in figure 7, it can be seen that a bandgap is achieved in the range of 500 – 700 Hz in which no particular resonance peak is observed. The stopband range is wider but less deep than the one that was initially calculated. These performances are obtained by only adding 20% of mass to the base plate.
In conclusion, considering the ease of manufacturing and the compactness of the resonator package this one could be a good option for future automotive applications in the NVH field for mass production [7].
Considering these aspects, it was chosen for the successive phases of the thesis.

3.4 Hollow parallelepiped local resonator solution

The metamaterial unit cell considered in this case is composed by a host structure and a local resonator "with a cantilever beam design that permits to tune the first out-of-plane bending mode frequency" [14].
Its structure is a parallelepiped with a hollow cylindrical section as represented in figure 8, with the dimensions of width, depth, height, and diameter of the pin reported in table 1.

dimension	symbol	value (mm)
depth	l	25
height	h	10 < h < 25
Width	w	10 < w < 25
diameter	d	0 < d < h
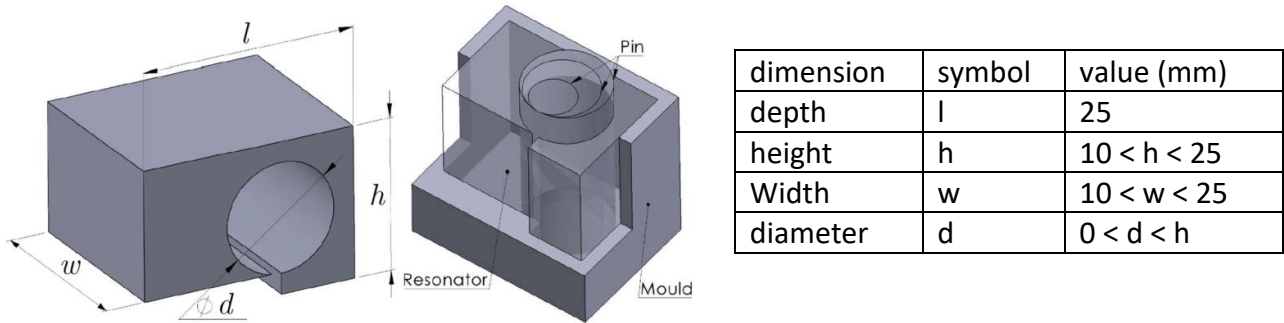
Figure 8: Resonator design (left), and mould for manufacture where variable pin diameter is shown (right).

The host structure is made of mild steel with a thickness of 2.4 mm while the local resonator is made of photopolymer manufactured by means of injection moulding or vacuum casting.

It can be demonstrated that by varying the diameter of the pin while maintaining constant the overall package of the resonator element different bandgaps can be achieved since the material distribution between the spring and mass section is varied.
An important thing to notice is that the same mould can be reused for the fabrication of different resonators which means that a noteworthy cost reduction is obtained.
In order to assess its attenuation properties a unit cell bandgap analysis of different elements with different inner diameters was performed and the obtained results are reported graphically below.
The resonator and the host structure were respectively described with the quadratic solid and shell elements.
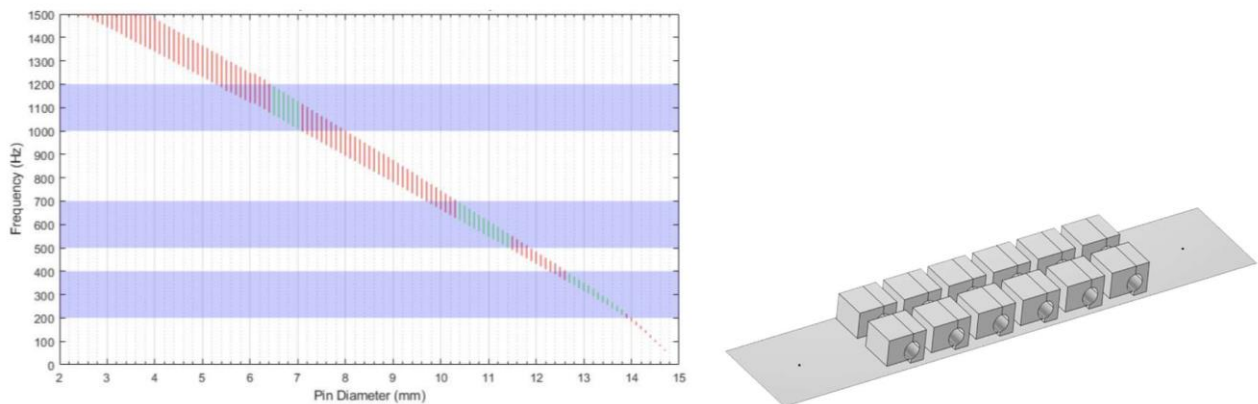
Figure 9: (left) Band gap frequencies as a function of pin diameter; metamaterial plate (right).

The vertical lines in the diagram represent the different bandgaps obtained from the corresponding pin diameter that is read on the x axis. So, it can be observed that a broad range of

frequency attenuation can be addressed which makes this solution particularly indicated for the purpose of NVH reduction in a vehicle. It can also be seen that a larger stopband is achieved for higher frequencies with respect to the lower ones.

Then, a metamaterial plate is numerically simulated by exciting it on one edge and measuring the FRF on the other edge. For the treated case a configuration (figure 9) of 12 unit cell with internal diameters of 6,7 mm, 10.3 mm and 13 mm was chosen.
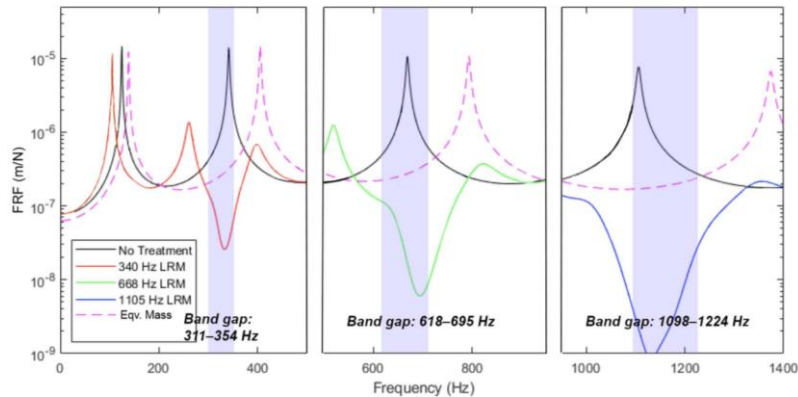
Figure 10: Low (311–354 Hz), mid (618–695 Hz) and high-frequency (1,098–1,224 Hz) performance of LRM designs are shown with respect to the untreated host structure and equivalent mass of the 1,105 Hz case.

From the above diagram it can be observed that the bending modes of the untreated host structure are attenuated of at least two orders of magnitude with a mass increase of the 20% that is a major result for what concern the vibration attenuation [14].

Considering these performances, the wide range of frequency that can be addressed, the simplicity of the production process of the local resonator and the possibility to reuse the same mould for different resonators, this solution could be a good candidate for the NVH attenuation in the future.

3.5 Composite sandwich metamaterial with spiral resonators

The proposed application is studied both for vibration attenuation and for load bearing scenarios and it is manufactured by means of 3D printing technology for carbon fiber-reinforced plastics (SCFRPs) and continuous carbon fiber-reinforced plastics (CCFRPs).

The metamaterial unit cell consists in a plate with a spiral resonator composed by a mass and spiral spring, as shown in figure 11. It has a 20 x 25 mm sandwich structure with a hollow core and stiff skin plates.
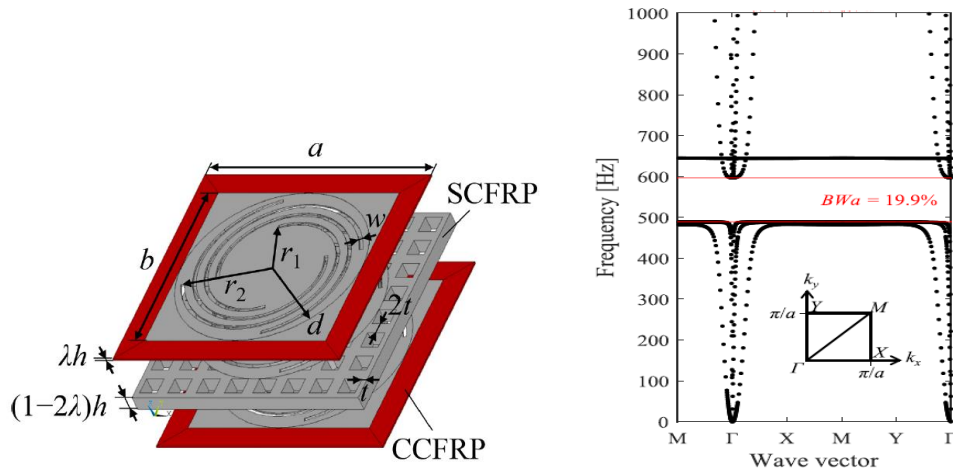
Figure 11: (left) Designs of unit cells investigated in this study; (right) Dispersion diagram of the unit cell.

By performing a unit cell analysis as described in paragraph 2, a stopband is observed between 480 and 600 Hz.

Then, a metamaterial plate with periodically displaced unit cell was analysed through FEM simulations considering the boundary conditions reported in figure 12.

The frequency responses "were obtained for three cases: the x directional output for a x-directional input, the y-directional output for a y-directional input, and the z-directional output for a z-directional input. A constant loss factor of 0.01 was used" [4].

As the diagram in figure 12 shows, there is a decrease of the transmissibility in the bandgap region for both the x, y and z directions. In particular, a bigger vibration attenuation can be noted along the z direction with respect to the other ones.
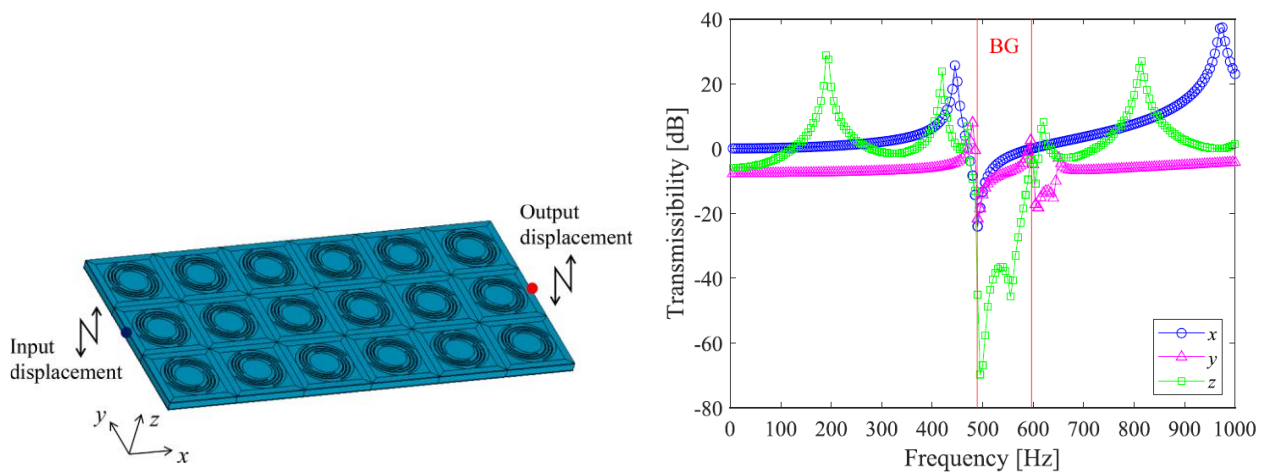
Figure 12: (left) FEM model of the frequency response analysis for the metamaterial plate; (right) transmissibility of the vibrations in the x, y, and z directions of the metamaterial plate.

Then a metamaterial plate was experimentally tested by hanging up the plate to an elastic tread, putting two accelerometers at its ends and exciting it with a shaker in the input measuring point. The results confirm the expectations of the numerical analysis although a lower attenuation is observed [4].

3.6 Single cantilever beam local resonator metamaterial

 In the proposed case study, it is considered a duct as a host structure that represent a one-dimensional transmission path. it is modelled as rectangular and non-fluid loaded duct, in order to reduce the required computational cost.

The local resonator, instead, has a cantilever beam body realized in PMMA with a mass located on its final part and a horizontal support at the bottom to link it with the host structure.
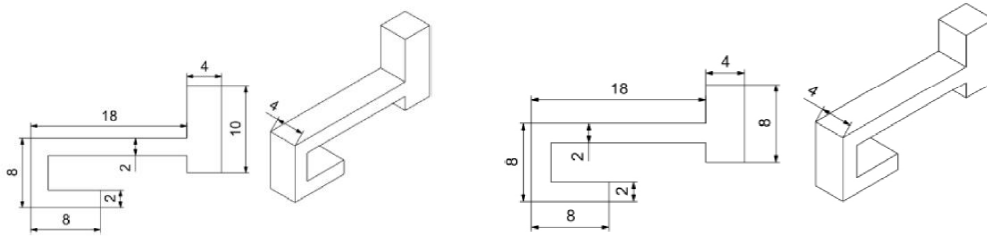
Figure 13: local resonator A and B design.

For the evaluation of the dispersion curves, five different configurations were considered:
- "Original configuration: duct without resonant structures, used as benchmark case.
- Configuration A: duct with 640 resonant structures of type A;
- Configuration B: duct with 640 resonant structures of type B;
- Configuration half A: duct with 320 resonant structures of type A as shown on the left of figure 14;
- Sequential configuration: duct with 320 resonant structures of type A on the first half of the duct and 320 resonant structures of type B on the second half;
- Mixed configuration: duct with 320 resonant structures of type A and 320 resonant structures of type B mixed as shown on the right of figure 14" [15].
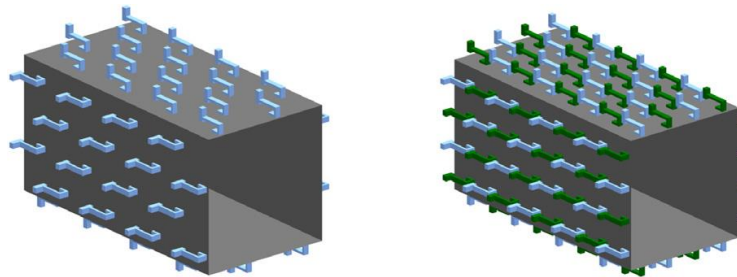
Figure 14: Visualization of the resonant structure lay-out for the half A configuration (left) and the mixed configuration (right).

For what concern the experimental test setup instead the duct is freely suspended, a roving hammer solicitation is utilised, and the considered response is the RMS acceleration measured in four different sections.
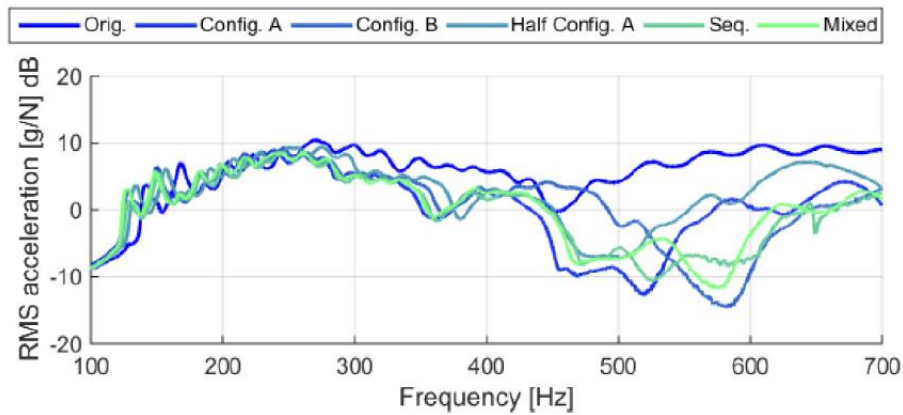
Figure 15: experimental test results

From the dispersion curves but also from the experimental tests results (figure 15) of the different configurations, it can be seen that in the mixed and sequential configurations the attenuation has an overall wider range of frequency, but it is less pronounced with respect to the configurations in which only one of the resonators is present. In particular for the mixed one two different bandgap can be noted with a higher mitigation with respect to the sequential configuration, which in turn has more constant trend [15].
The latter could be the most interesting solution in NVH automotive field among all the configurations in the paper.

3.7 Cantilever beam with endpoint mass local resonator metamaterial

In this paper it is presented a case study with a host structure characterized by multiple transmission paths, that is a representing case of when a portion of vehicle body is solicited by a shock absorber. The metamaterial host structure is composed by a steel plate composed by four parts, as shown in figure 16, in which the elements ② and ③ represent two different transfer paths. The local resonator, instead, has a cantilever beam body realized in PMMA with a steel mass glued on final part and a horizontal support at the bottom to link it with the host structure.
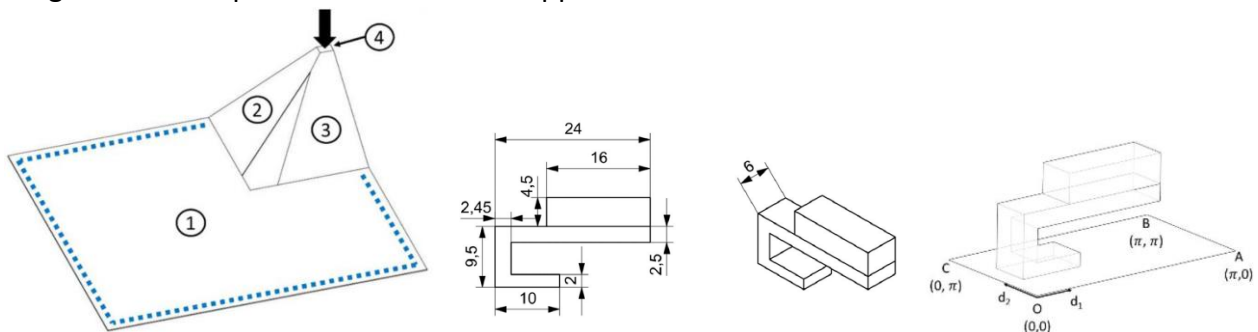
Figure 16: (left) Representation of the host structure with the force location on part ④ (black arrow) and the measurement points (blue dashed lines); (right) local resonator design and Irreducible Brillouin Contour.

By performing a unit cell analysis according to the methodology in paragraph 2, a stopband can be noted in the region between 291,6 Hz and 322,6 Hz with respect to the untreated host structure, as shown in figure 17.

Then, it was performed the experimental validation for a freely suspended steel plate, with a shaker located in the part ④ and 67 measuring points situated along the edges of element ①, represented by the blue points in figure 16.
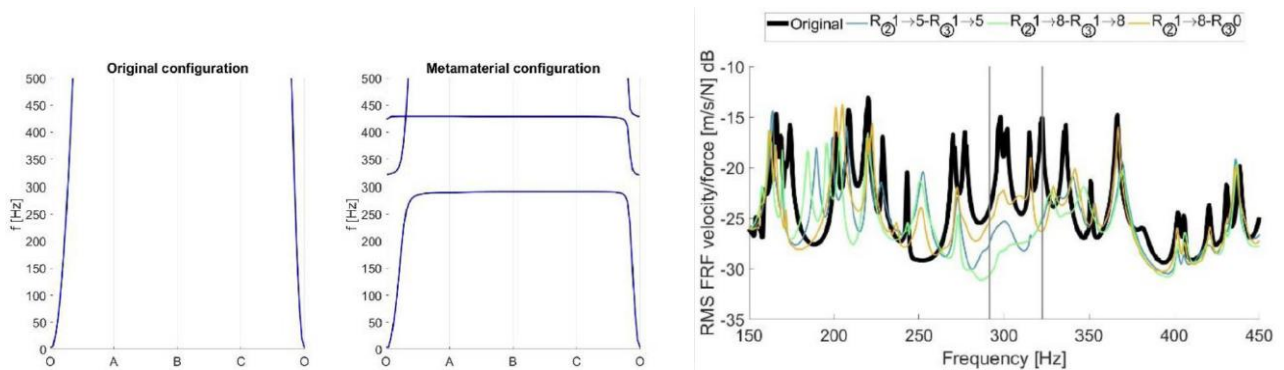
Figure 17: (left) Dispersion diagrams for the bare structure, and for the metamaterial UC; (right) RMS FRF velocity/force of the host structure in original configuration and configuration A and configuration B.

The results in figure 17, show that for the treated case, an attenuation is observed with respect to the host structure, not only in the bandgap range but also around it. The obtained average mitigation is equal to 6.8 dB when the mass is increased by the 2,4%. Other than that, the resonant frequencies before the bandgap are largely shifted towards lower values, while the same effect is almost not present after the stopband [16].

This application, unlike other ones, require a reduced covering of the resonator over the host structure and thus lower mass is added making it well suited for compact and particularly lightweight applications. In addition to this, it has the positive feature of being easy to produce, which makes it a good option for NVH reduction.

4. Acoustic applications

Helmholtz resonators

4.1 Microperforated plate metamaterial

The proposed solution consists in a micro perforated aluminium panel as a host structure with local resonators composed by a silicon rubber spring connected with a mass, displaced over its surface. Under the plate there is an air backing cavity and a rigid border. The boundary conditions are rigid clamping on the edges with a normally incident plane wave.
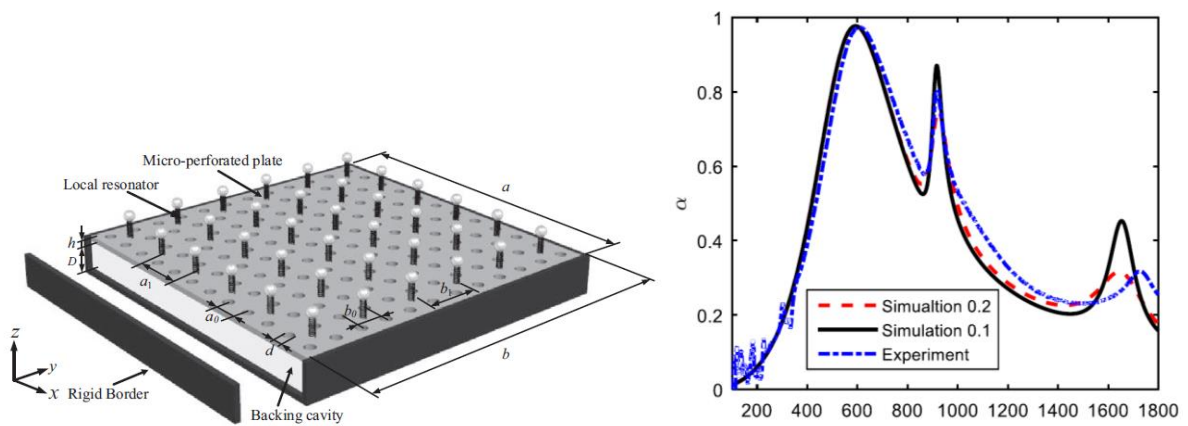
Figure 18: (left) Configuration of the flexible metamaterial panel; (right); The absorption of the flexible metamaterial panel under clamped condition.

To study its attenuation performances a plate simulation has been performed in the COMSOL software. In particular, they were used the multiphysics modules of solid mechanics, pressure acoustics, and thermoviscous acoustics. The metamaterial panel is modelled with the first module while the second and third ones respectively describe the incident sound pressure wave and the air inside the microperforations. For what concern the experimental validation, a metamaterial plate is realized and tested in an impedance tube with a two-microphone method.
The obtained results reported in figure 18, show for both FEM simulation and lab test that three different absorption peaks are present, respectively at 608 Hz, 926 Hz and 1663 Hz. The first one is due to the rigid plate and the other two are due to the local resonator. It is worth to note that although the third peak is outside the frequency range of interest for automotive applications, it can be shifted (along with the second one) towards lower frequencies by tuning differently the local resonator frequency, by adding a larger number of resonant structures, or changing the edges boundary conditions from clamped to simply supported [17].

4.2 SONOBEX Noise Trap panel

The proposed solution consists in the SONOBEX Noise Trap panel, characterized by a unit cell which is composed by two C shaped steel structures with a neck in the middle.
The metamaterial unit lattice is tested on COMSOL software under the hypothesis of infinite length along the x axis, represented by a perfectly matched layer on both sides.
For what concern the boundary conditions, an acoustic pressure field is applied on one side, with its initial acceleration and velocity at the edges set equal to zero. The metamaterial perimeter is instead defined as sound hard wall with a periodic boundary condition imposed along the x axis. Then, a parametric sweep of the element length is performed, and the transmission loss is calculated. The obtained results are shown in figure 19.
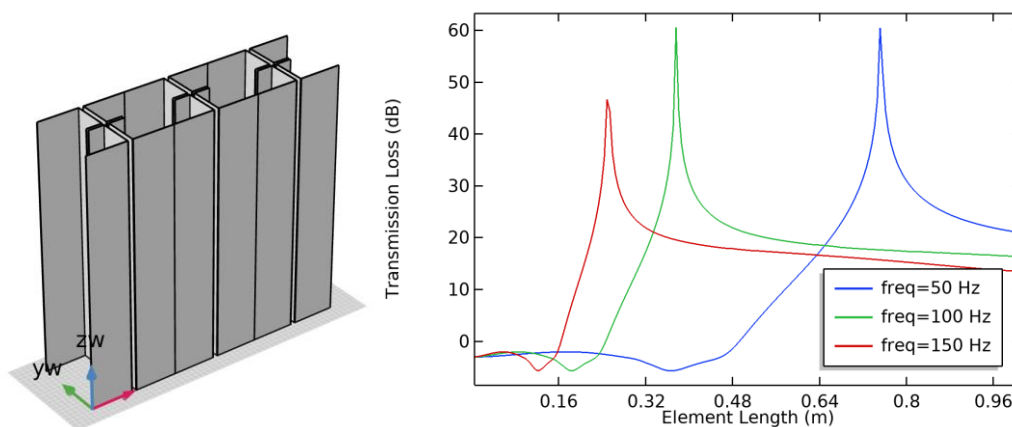
Figure 19: (Left) Geometry of the Noise Trap Panel; (right) Transmission Loss optimization plot.

From the diagram it can be noted that 50 Hz, 100 Hz and 150 Hz frequency are attenuated with a peak of 61.7 dB, 60.9 dB and 46.91 dB, respectively. Considering the metamaterial working frequencies and performances, it could find application in vehicle NVH attenuation.
It is important to point out that in order to achieve a more compact design to fulfill automotive constraints, the element length for example can be reduced if contemporarily the neck length is increased along x axis while maintaining the same performances [18].

Mechanical resonators
4.3 Basic spring-mass resonator metamaterial

The considered solution consists in an aluminium plate host structure with a 5 cm x 5 cm periodically displaced spring-mass resonators over its surface. In order to study its acoustic attenuation performances, following the methodology in paragraph 2 for the infinite periodic structure, the dispersion curves and sound transmission loss are evaluated.
For the STL calculation, it is used the hybrid Wave Based - Finite Element UC method, in which the structural FE unit cell model is coupled to two semi-unbounded periodic acoustic wave-based domains, one above and one below the structure.

The numerical model for the above-mentioned unit cell is composed by 100 shell elements. For the finite structure STL evaluation a simply supported boundary condition with an incident acoustic plane wave as an excitation are applied.

Figure 20: (left) bending wave dispersion curves; (right) Normal incidence STL for the infinite periodic LRM.

In the dispersion curves, taking into account the out-of-plane flexural waves that are more important in acoustics, a bandgap can be noted in the range 445–644 Hz, obtained from a mass addition of the 80%.

In the STL diagram, instead, it can be seen a peak in the stopband region and in particular around the resonator frequency, where the metamaterial has better performances with respect to the homogeneous bare structure (ρ_{host}) and the configuration with a mass equal to the sum of the structure and resonators masses ($1.8\rho_{host}$). The same trend is confirmed for the finite plate FEM simulation [19].

4.4 Two cantilever beam metamaterial

Considering that low frequency structure borne noise in vehicle cabin is mainly due to by tire/road interaction while driving, a metamaterial application is studied to address the issue.

The proposed solution unit cell is characterised by a local resonator with a mass-spring-damper system, composed by two cantilever beams with an end point mass at the two extremities, as shown in figure 21. It is worth noting that by varying the endpoint masses different resonant frequencies can be achieved. The chosen material is polyamide, which is processed with selective laser sintering technique.

Figure 21: (left) local resonator design; (right) dispersion curves for the unit cell.

For what concerns the case study, it was opted for a European SUV with a MacPherson Strut as rear suspension and tires model 235/60 R18. In this subsystem, vibrational energy enters inside vehicle body at a frequency around 190 Hz. So, the metamaterial was tuned at a resonant frequency of 193 Hz.

Exploiting the methodology described at paragraph 2, a unit cell analysis is performed. The resonator was described with the linear solid element property, while its base was modelled as clamped to the host structure. The latter was assigned the steel material property and the flat plate element characteristics.

From the obtained dispersion diagram in figure 21, bending (B), shear (S) and longitudinal (L) free wave can be noted. For the bending waves a complete bandgap from 193.1 Hz to 224.1 Hz is observed, while for longitudinal and shear waves only partial stopband is achieved, in the same frequency range, along the d2 and d1 direction respectively.

In the lab validation test the bare structure, the configuration with TVA and the metamaterial treated one were tested. For the treated case, two metamaterial patches are built and placed in the rear shock towers region, with a 48% mass reduction with respect of the conventional solution.

A shaker is connected to rear right and rear left bottom part of the suspensions, which are excited one at the time with a random white noise excitation. As an objective, the SPL is evaluated with three microphones at driver right ear (represented with letter D in the diagrams), front passenger left ear (FP) and rear right passenger left ear (RP) positions.
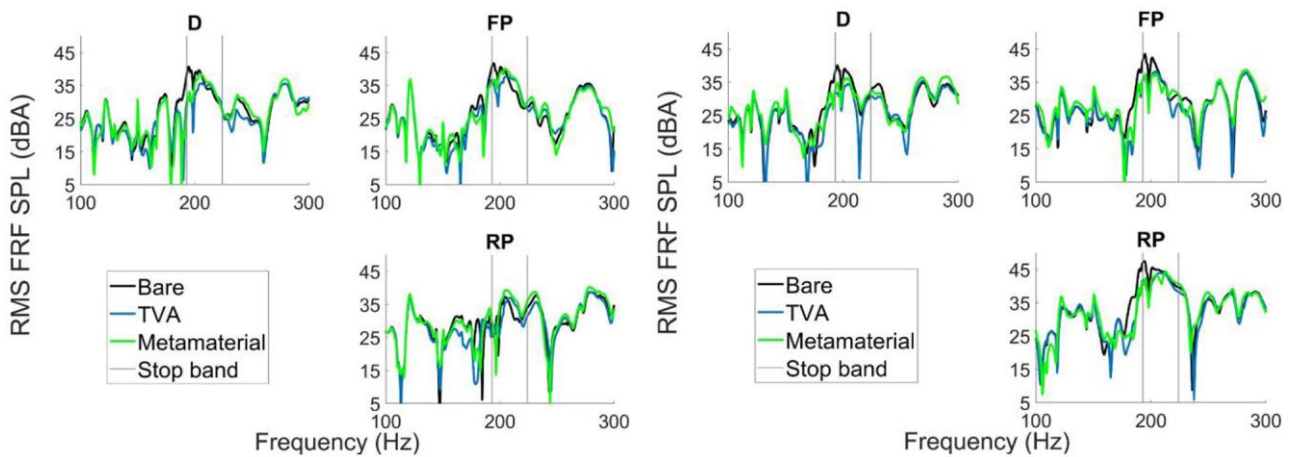
Figure 22: RMS FRF SPL comparison among the three tested configurations, when the source of excitation is the under the rear left (diagrams on the left) and rear right suspension (diagrams on the right).

From the diagrams It can be observed that when the left shock tower is excited, the treated configuration shows an acoustic improvement with respect to the bare structure in the range of 185-210 Hz. It has comparable performances with respect to the TVA configuration for the frequency range from 185 Hz to 200 Hz, but it performs worse with respect to the TVA configuration. When an excitation on the right shock tower is present, instead, the metamaterial configuration has similar noise reduction capability as for the TVA configuration in the 185-210 Hz range. Other than that, the metamaterial configuration has a notable SPL reduction right before and at the lower bound of the predicted stop band.

Finally, an on-road test is performed on asphalt road at 50 km/h and on a cobblestone road at 20 km/h. The obtained results confirmed acoustic improvements around the stopband region for the treated configuration. [20].

Considering the ease of manufacturing for the proposed metamaterial solution, its performances and its capability of being easily tuned at different resonant frequencies, it was chosen for the successive phases of the thesis.

4.5 Two separated beams local resonator metamaterial

An initial experimental test of a hatchback vehicle on a dynamometer in a semi-anechoic room is performed in order to evaluate the tire acoustic resonances at different vehicle speeds of 40, 50 and 80 km/h. From the obtained SPL diagrams, two resonant frequencies were evaluated, at about 224 Hz and 238 Hz, respectively. Results also showed that the rear wheels excitation contributes more than the front one. So, a metamaterial solution is designed with a local resonator characterized by two different cantilever beams with an endpoint mass and a clamped base. The chosen material is a martensite-hardenable steel manufactured with 3d printing technology. One of the two cantilever beams has the first out-of-plane bending mode set at 225 Hz and the other one is set at 238 Hz. For wat concerns the numerical modelling, the resonator was described with the quadratic solid element and the host structure with the quadratic shell element.
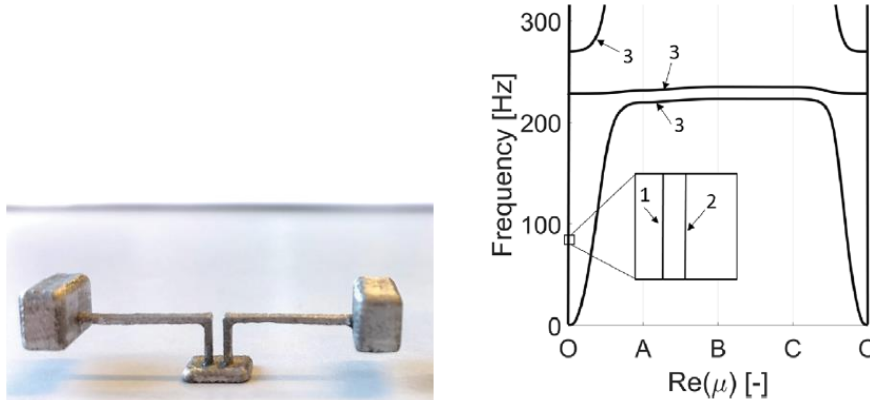
Figure 23: unit cell design (left) and dispersion curves (right)

From the unit cell analysis results reported in figure 23, two bandgaps for out-of-plane bending waves (3) are found between 227–243 Hz and 243–273 Hz. No stopband for plane waves (1 and 2) is noted.
Then, the metamaterial was built and experimentally tested under the same conditions of the initial first test, for three different vehicle speeds, 40, 50 and 80 km/h. The ΔSPL quantity was introduced as the difference between bare configuration SPL and the metamaterial solution SPL. A positive ΔSPL indicate a noise radiation reduction.
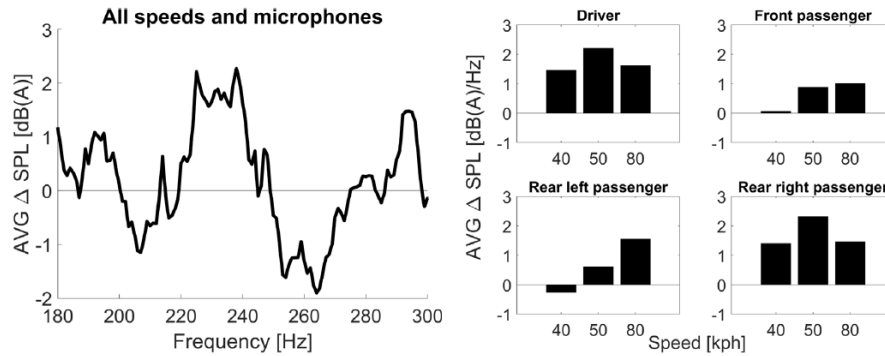
Figure 24: Average ⊿SPL (left) and band average ⊿SPL (right) calculated between 220–250 Hz.

In the diagrams, the averaged SPL over all the vehicle speeds and passengers' positions is represented. The results confirm the predicted stopband in the 220-250 Hz with an acoustic improvement of about 2 dBA, which is less than what was numerically evaluated. As the band average diagram also demonstrates, the improvement varies with the position and the vehicle speed, since the tire resonance frequency varies with it [21].

4.6 Single-stage multi-degree-of-freedom resonators

The considered metamaterial unit cell is composed by an aluminium host structure with a single stage multi degree of freedom resonator. The latter consists of a lumped mass and four springs, two of them have a stiffness along the x axis and the other two have a stiffness along the y axis. The x-y unit cell dimensions are 3 cm x 3 cm.

The NVH material properties are studied on the Ansys software. Here, for simplicity, the stiffnesses of the spring elements in the y direction are assumed as null.
The attached mass is modelled as a homogeneous beam using BEAM 188, while the springs are described with COMBIN 14 characteristics, and SHELL 181 is used for the host plate. The property MPC184, instead is used for the connecting point of the springs.
A plate analysis is performed when a harmonic force in the point (0.1 m, 0.1 m) and the response is measured in the point (0.4 m, 0.3 m).

Vibration performances
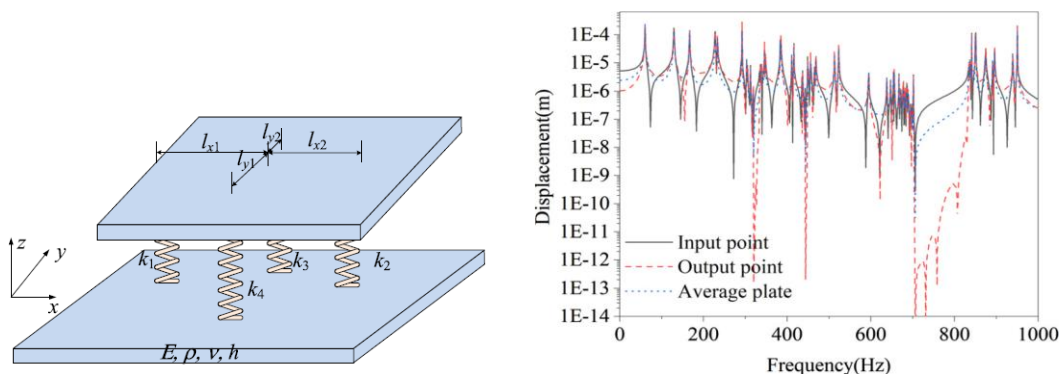
Figure 25: (left) Diagram of a unit cell of the metamaterial plate; (right) Vibration response of the metamaterial plate.

23

From the obtained diagram of the mobility displacement, which is an index of the vibrational behaviour of the plate, they can be seen three different regions at about 310 Hz, 440 Hz and 750-800 Hz, in which the curve has a notable reduction, that are the metamaterial bandgaps. Other than that, it can be noted that the first and second stopband is tighter than the third one, although their vibration reduction performances are similar [22].

Acoustic performances
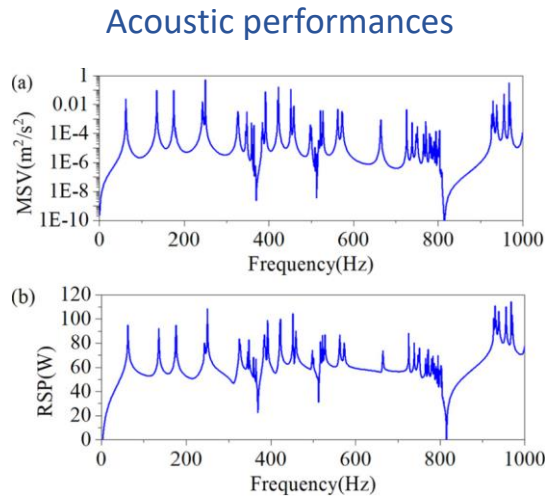
Figure 26: MSV and RSV of the metamaterial plate

Then, it was evaluated the mean square velocity (MSV) and radiation sound power (RSP). The curves have similar trend among each other, and three different dips can be noted under 1000 Hz. This shows that, as long as we work in the stopband regions both noise reduction and vibration mitigation can be achieved [22].

Although this solution has not been experimentally tested and validated, the numerical results suggest that it could be a good option for vehicle applications, since not only it has both noise and vibration attenuation, but it also has three different bandgaps that permit to reduce NVH phenomenon not only at low frequency but also at medium and high frequency.

4.7 Low-Frequency Acoustic Metamaterial plate

From a test drive of a hatch car that is running on a rough road surface at the constant speed of 30 km/h, it is found that the measured output of the sound pressure level at the driver's right ear and at the middle of the back passenger seat have a peak at 35 Hz.
From the subsequent numerical analysis of the joint contribution of the body parts, it is established that this peak of noise is mainly due to rear door contribution. So, in order to reduce it a metamaterial solution is designed.
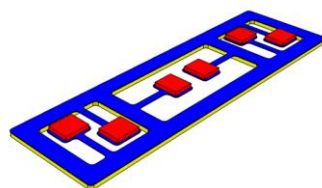
Figure 27: unit cell design

Its unit cell is composed by an acoustic metamaterial matrix plate coloured in blue in figure 27, an adjustable mass block represented in red and an acoustic metamaterial damping layer in yellow. The metamaterial is placed on the sheet metal parts of the tailgate through the magnetic damping layer.

It is wort to make notice that the mass block and the cantilever beam in the metamaterial form an acoustic spring-mass system which permits to tune the band gap frequency by varying the mass block. Then a full vehicle FEM analysis is performed in Hypermesh and the evaluated responses are the sound pressure level in the driver's right ear, the one in the rear passenger's seat and the vibration acceleration in the middle of the tailgate panel.

Acoustic performance
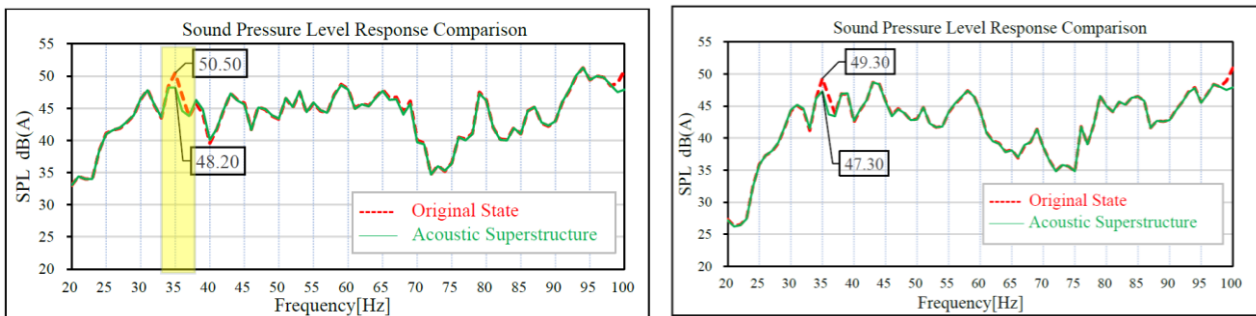
Figure 28: (left) Comparison of sound pressure levels in the middle of rear passenger row and in the driver's right ear (right).

From the comparison diagrams between the original and the treated case, there is a notable reduction in the 35 Hz noise peak. In particular, the SPL amplitude in the driver's right ear and in the middle of the passenger rear row is reduced of 2 dBA and 2.3 dBA respectively.

Vibration performances
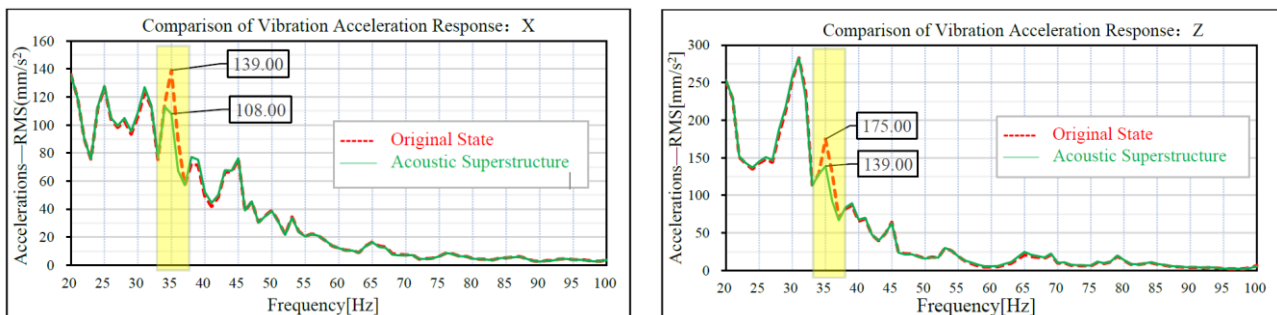
Figure 29: Comparison of x-direction and z-direction vibration response of sheet metal parts of tail door.

From the graphs between the treated and untreated structure it can be seen a major acceleration reduction around the 35 Hz frequency region both along the x and z axis. This means that also a vibration attenuation is achieved [23].

Although this metamaterial has not been experimentally tested, it is a promising solution for NVH automotive field if we consider its performances and the fact it can reduce both noise and vibration.

5. Developed numerical model

5.1 Procedure

After the initial literature review a numerical model for the evaluation of the dispersion curves was developed and validated.

The chosen metamaterial applications for the simulations were the one with two cantilever beam reported in paragraph 4.4 and its host structure and the one with the T shaped local resonator described in paragraph 3.3.

Initially, the unit cells were modelled in Altair Inspire and were imported in the COMSOL software.

Here, after assigning material properties to the 3D model, the Bloch-Floquet periodic boundary conditions were applied to the relevant parallel faces of the unit cell [24], as shown in figure 30. In these boundary conditions it has been specified the wavenumber vector k components along the x and y axis, defined in the parameter ribbon according to the Irreducible Brillouin Contour of the considered metamaterial.

Since the dispersion diagram are periodic with a periodicity of 2π /s, where s is the distance between the above-mentioned parallel faces, "in the reciprocal-lattice space the interval $-\frac{\pi}{s} < k < \frac{\pi}{s}$ would be known as the 1st Brillouin zone, and every 2π /s interval outwards from the 1st zone would be the 2nd, 3rd, 4th, and so on. The 1st zone is usually the focal point because the dispersion curves are the same in other zones when the periodicity is simple" [24].

The Irreducible Brillouin Contour is basically the 1st Brillouin zone reduced by all of the symmetries in the point group of the lattice. For example, for a square unit cell, the IBC is represented by the purple triangle in the first quadrant, as represented in figure 31.
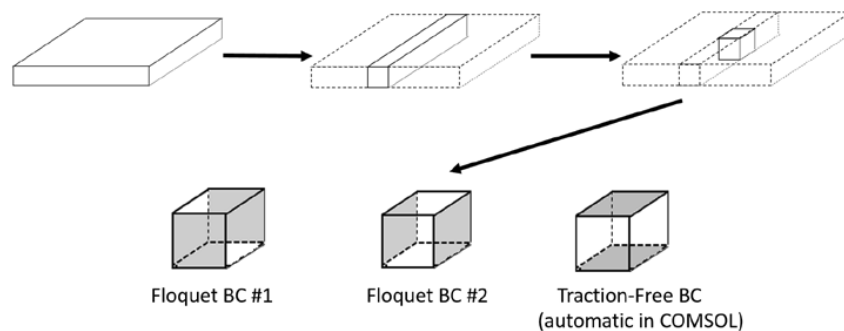
Figure 30: Concept image of how the infinite plate is constrained to a unit cell and how the boundaries are then defined.
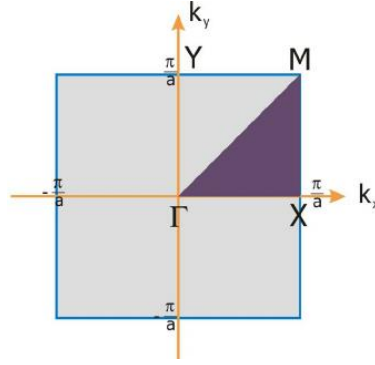
Figure 31: The 1ˢᵗ Brillouin zone (grey square) and the irreducible Brillouin zone (purple triangle) for a square lattice

Every edge of the contour represents a direction of propagation of the elastic wave and constitutes a slice of the entire dispersion diagram. The wave vector components are defined around this contour in function of the arbitrary user defined parameter "ii".

Then, a parametric sweep is set for this parameter in order to evaluate the dispersion curves, with a range from 0 to an integer value equal to the number of the propagation directions of the IBC.

For example, considering the same square unit cell as before, the ii parameter was swept from 0 to 3 and the k_x and k_y components were defined as:

$$
k_x(ii) = \begin{cases}
\dfrac{\pi}{s} * ii, & 0 < ii < 1, & \Gamma \to X \\[2mm]
\dfrac{\pi}{s}, & 1 < ii < 2, & X \to M \\[2mm]
(3 - ii) * \dfrac{\pi}{s}, & 2 < ii < 3, & M \to \Gamma
\end{cases}
$$

$$
k_y(ii) = \begin{cases}
0, & 0 < ii < 1, & \Gamma \to X \\[2mm]
(ii - 1) * \dfrac{\pi}{s}, & 1 < ii < 2, & X \to M \\[2mm]
(3 - ii) * \dfrac{\pi}{s}, & 2 < ii < 3, & M \to \Gamma
\end{cases}
$$

Below are reported the obtained dispersion diagram results.

5.2 host structure validation
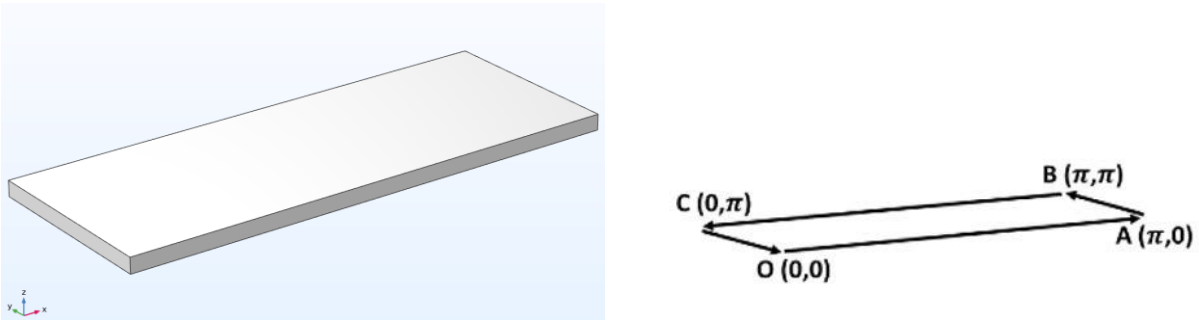
Figure 32: (left) host structure design; (right) Irreducible Brillouin Contour.
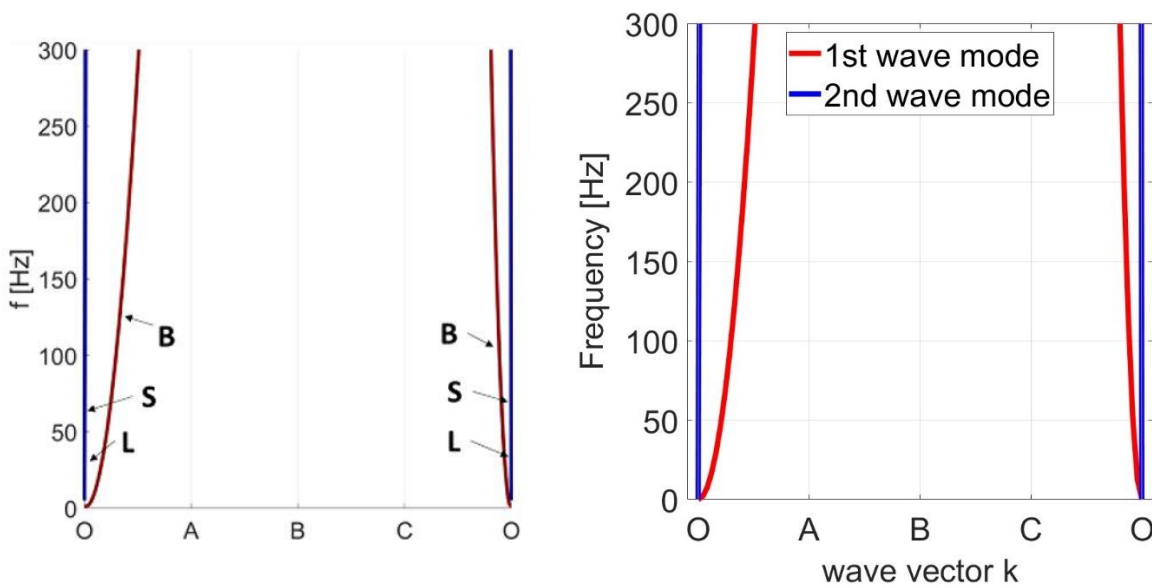
Figure 33: Dispersion diagram for the UC, consisting of the host structure only reported in the research paper (left) and numerically evaluated (right).

In figure 33 is reported the obtained dispersion diagram evaluated along the contour O, A, B, C, O that is $(0,0) \rightarrow (\pi,0) \rightarrow (\pi, \pi) \rightarrow (0, \pi) \rightarrow (0, 0)$, as shown in figure 32. The considered periodicity is 65 mm along the x axis and 25 mm along the y axis respectively. In the graph, different wave modes are indicated with different colours.

From the comparison of the evaluated dispersion curve with the one reported in the research paper we can see a confirmation of the correctness of developed numerical model.

In particular, no significant bandgap is observed along the considered contour.

5.3 Two cantilever beam metamaterial validation
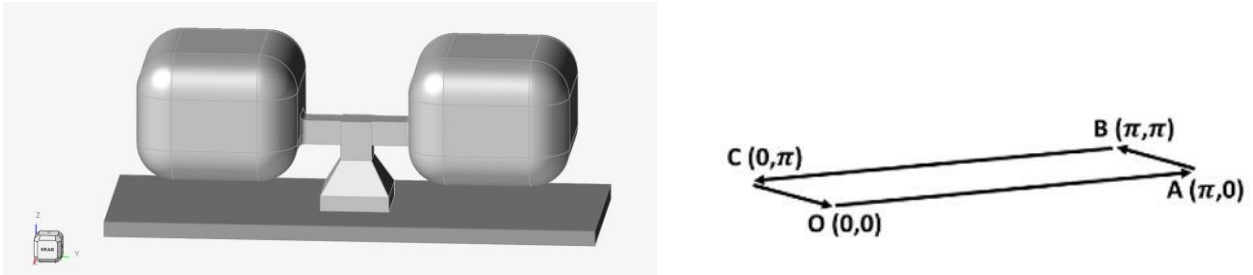
Figure 34 (left) two cantilever beam metamaterial unit cell design; (right) Irreducible Brillouin Contour.
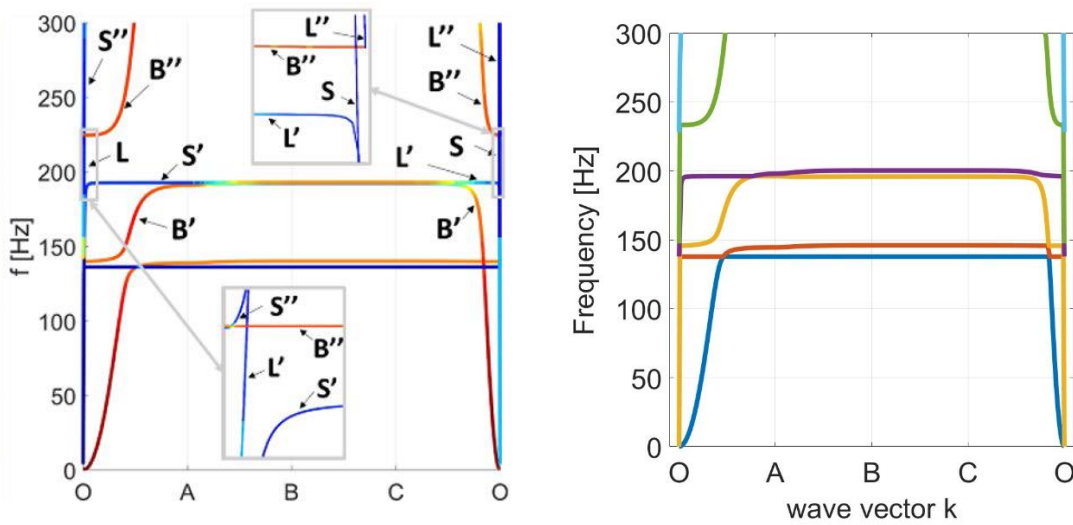
Figure 35: Dispersion diagram for the metamaterial UC, consisting of the host structure and of the local resonator reported in the research paper (left) and numerically evaluated (right).

In figure 35 is reported the obtained dispersion diagram evaluated along the Irreducible Brillouin contour O, A, B, C, O that is $(0,0) \rightarrow (\pi,0) \rightarrow (\pi, \pi) \rightarrow (0, \pi) \rightarrow (0, 0)$, as shown in figure 34. The considered periodicity is 65 mm along the x axis and 25 mm along the y axis respectively.
In the graph, different wave modes are indicated with different colours.

From the comparison of the evaluated dispersion curve with the one reported in the research paper we can see a confirmation of the correctness of developed numerical model.

In particular, a complete bandgap is observed for the 200 – 233 Hz frequency range.

5.4 T-shaped local resonator
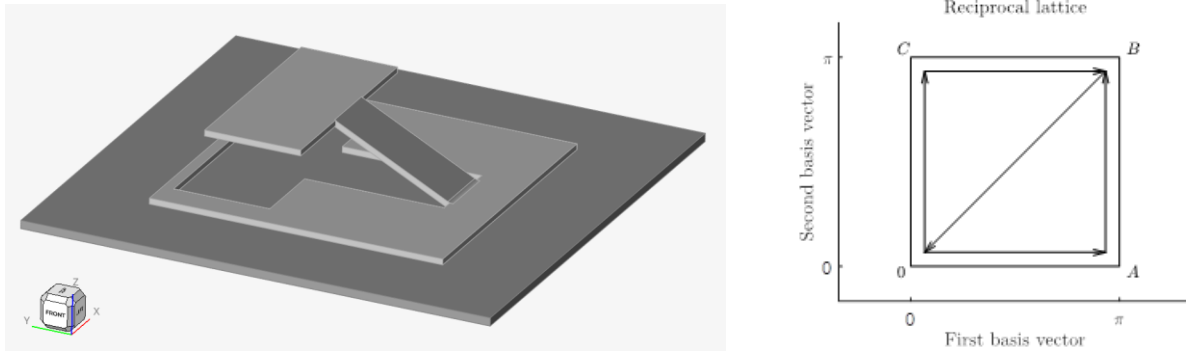
Figure 36: (left) T-shaped local resonator metamaterial UC design; (right) Irreducible Brillouin Contour.
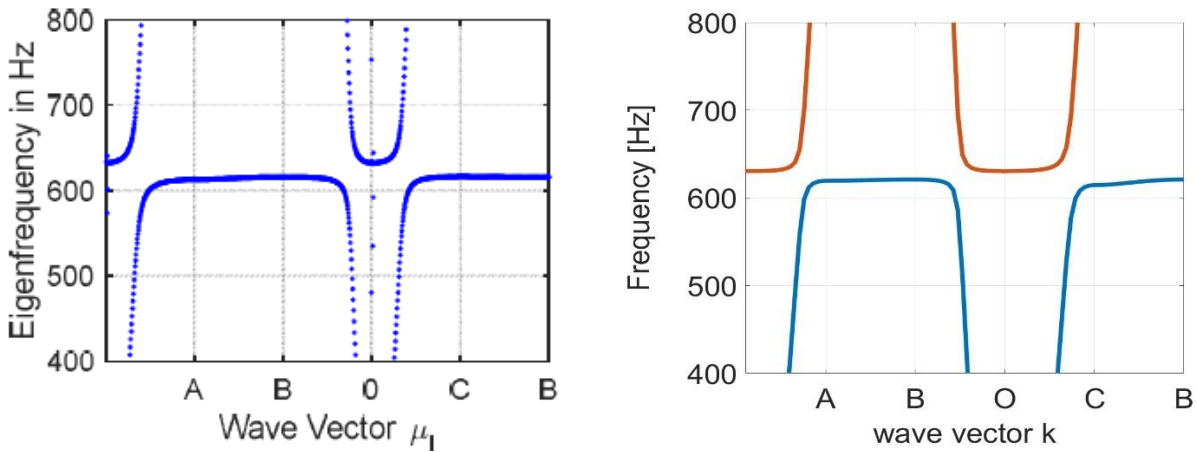
Figure 37: Dispersion diagram for the metamaterial UC, reported in the research paper (left) and numerically evaluated (right).

In figure 37 is reported the obtained dispersion diagram evaluated along the Irreducible Brillouin contour O, A, B, O, C, O that is $(0,0) \rightarrow (\pi,0) \rightarrow (\pi, \pi) \rightarrow (0,0) \rightarrow (0,\pi) \rightarrow (\pi,\pi)$ as shown in figure 36. The considered periodicity is 40 mm for both the x and y axis.

In the graph, different wave modes are indicated with different colours.

From the comparison of the evaluated dispersion curve with the one reported in the research paper we can see a confirmation of the correctness of developed numerical model.

In particular, a complete bandgap is observed for the 620 - 635 Hz frequency range.

6. Topology optimization

6.1 Unit Cell design

Initially, it was decided to conduct some preliminary simulations with different unit cell design and see how the bandgap is influenced. So, the first UC configuration is characterized by the same resonant structure of the research paper [7] with an added mass made of steel whose dimensions are 7,5 mm x 18 mm x 1,25 mm [7]. The same material (aluminium, for the local resonator), Irreducible Brillouin Contour and periodicity (40 mm along both the x and y axis) were considered for the following cases. The local resonator thickness is instead equal to 0.5 mm.
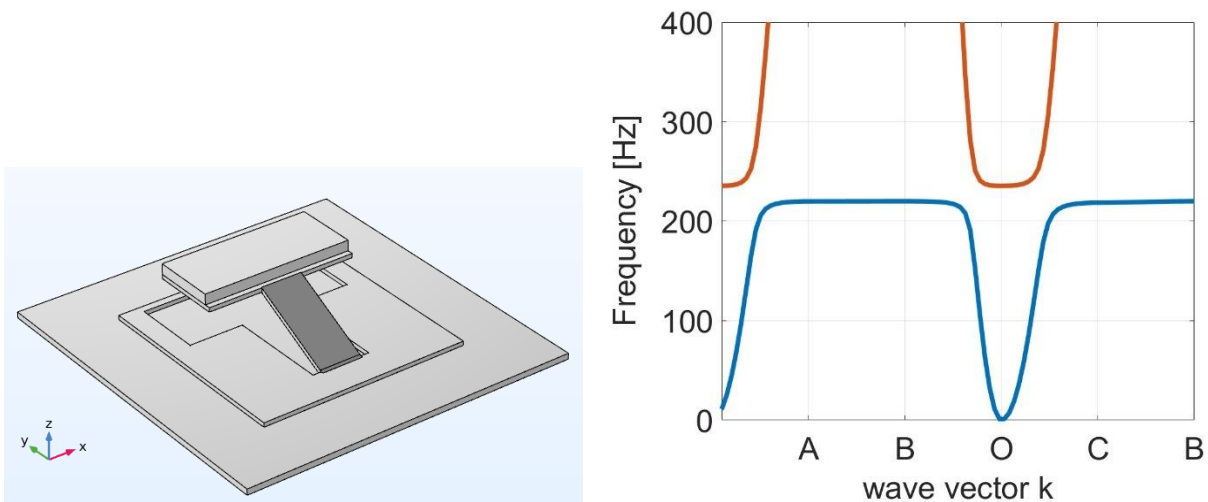
Figure 38: (left) unit cell design with the added mass; (right) dispersion curves of the unit cell.

From the obtained dispersion curves reported in figure 38, the stopband is evaluated between 220 Hz and 235 Hz. So, this configuration has the same bandgap width of the original configuration, but it is shifted towards lower frequencies with respect to it.

Then, it was decided to make the unit cell completely flat, for ease of manufacturing. A square spacer plate was put between the host and the resonant structures to prevent the resonator from hitting the host structure. The obtained simulation results are reported below.
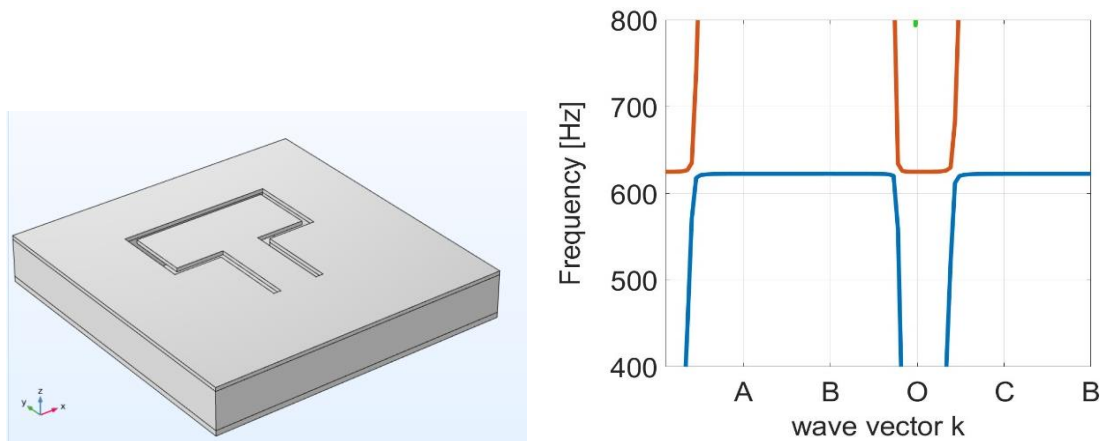
Figure 39: (left) modified unit cell design; (right) dispersion curves of the unit cell.

Unfortunately, the evaluated bandgap was reduced in width from 615-625 Hz to 622-627 Hz with respect to the original case study. For this reason, it has been chosen to not test this unit cell configuration any further and to realize a different UC concept.

In the new design it was removed the steel host structure and the spacer plate, while the resonator was kept the same as before.
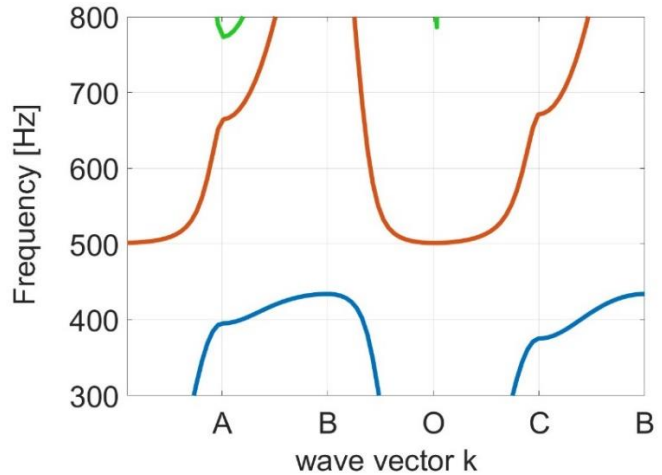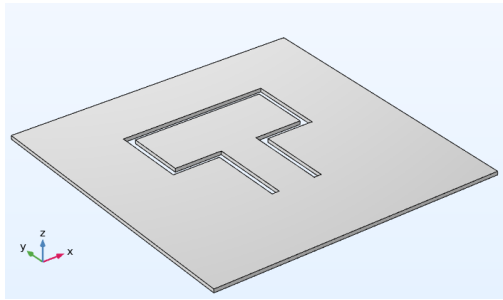
Figure 40: (left) final unit cell design; (right) evaluated dispersion diagram for the 40 mm periodicity unit cell.

As it can be seen from the diagram above, it is found a bandgap between 432 - 500 Hz, which is particularly wide. For this reason, it has been decided to perform the topology optimization basing on this cell configuration.

6.2 Periodicity topology optimization

As a first step, it has been varied the x and y axis reciprocities from 40 mm to 50 mm and 60 mm, keeping all the other geometrical quantities constant, and see how the bandgap is affected.
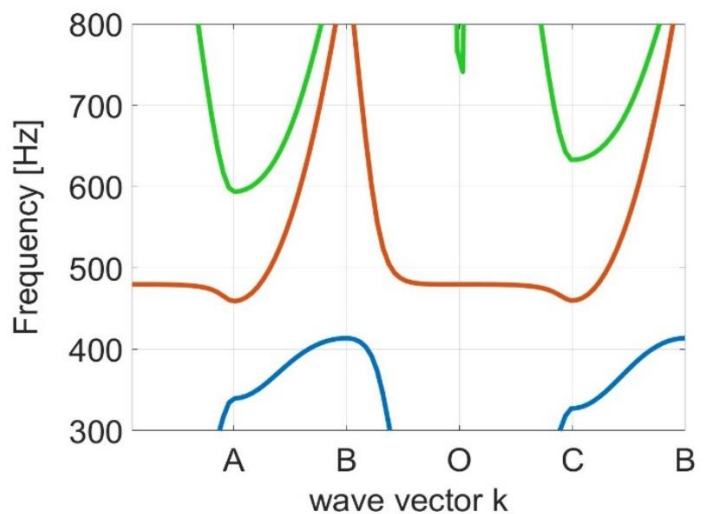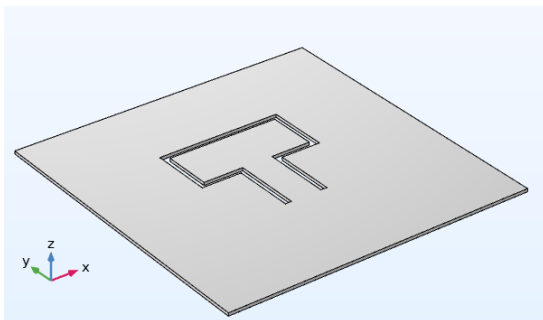
Figure 41: (left) unit cell design with a periodicity of 50 mm; (right) dispersion diagram for the 50 mm periodicity UC.

From the obtained graph it can be noted a bandgap between 411 and 460 Hz, which is narrower and shifted towards lower frequencies with respect to the original case study. Other than that, it

can be seen a major influence of the third wave mode (represented in green in the diagram) in the considered frequency range.
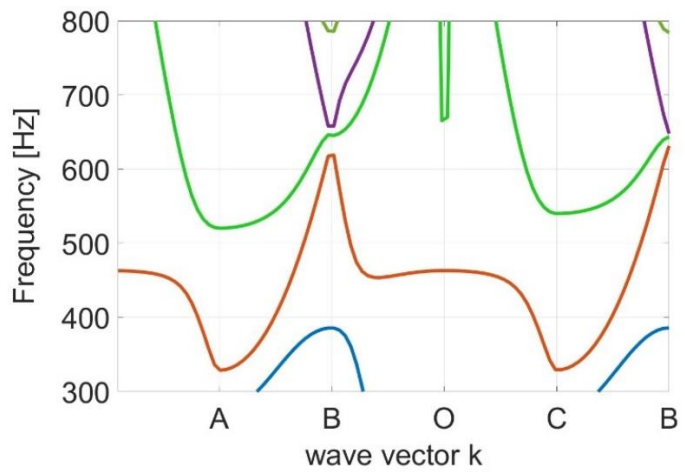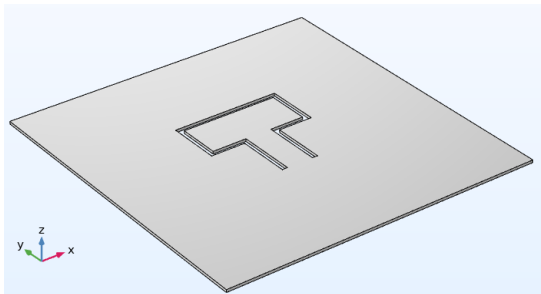
Figure 42: (left) unit cell design with a periodicity of 60 mm; (right) dispersion diagram for the 60 mm periodicity UC.

As it can be noted from the diagram, for the 60 mm periodicity unit cell design, there isn't any complete bandgap, but only some partial ones.

So, taking into account the obtained results, it was chosen, instead, to reduce the x and y axis periodicities and see how the bandgap changes in function of it. The considered periodicities were 35, 30 and 25 mm.
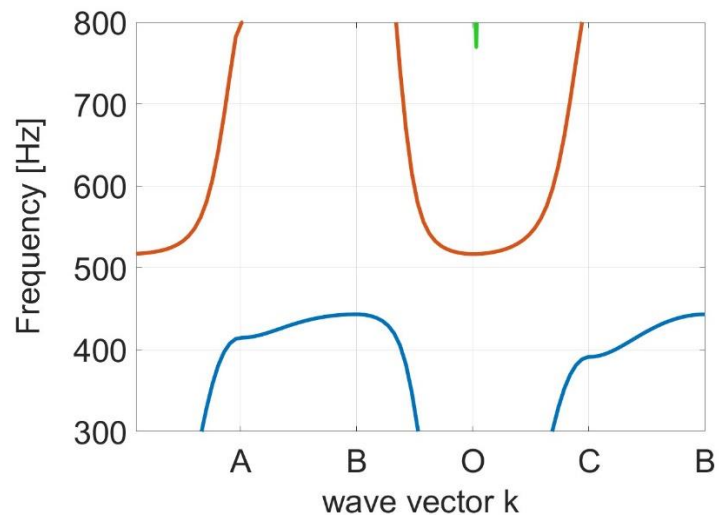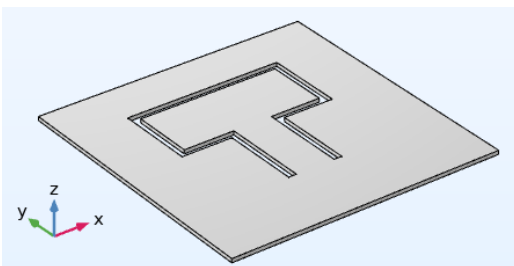
Figure 43: (left) unit cell design with a periodicity of 35 mm; (right) dispersion diagram for the 35 mm periodicity UC.
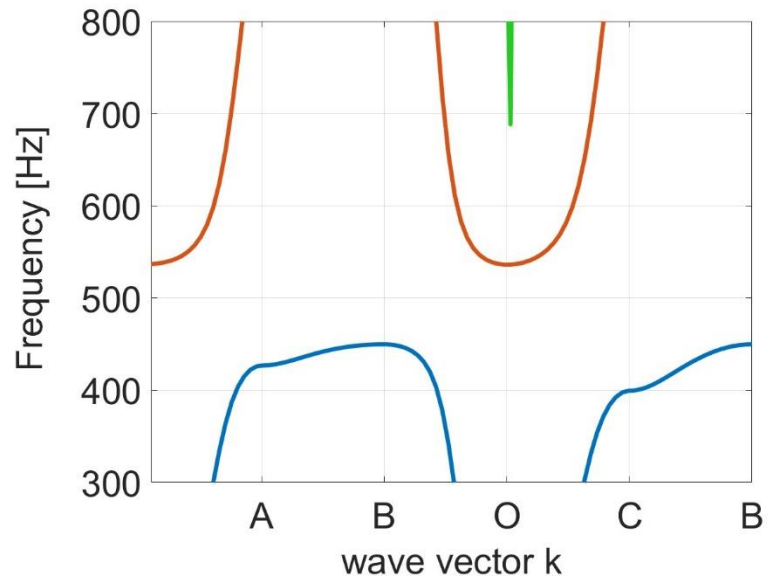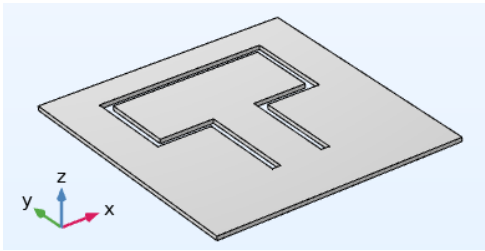
Figure 44: (left) unit cell design with a periodicity of 30 mm; (right) dispersion diagram for the 30 mm periodicity UC.
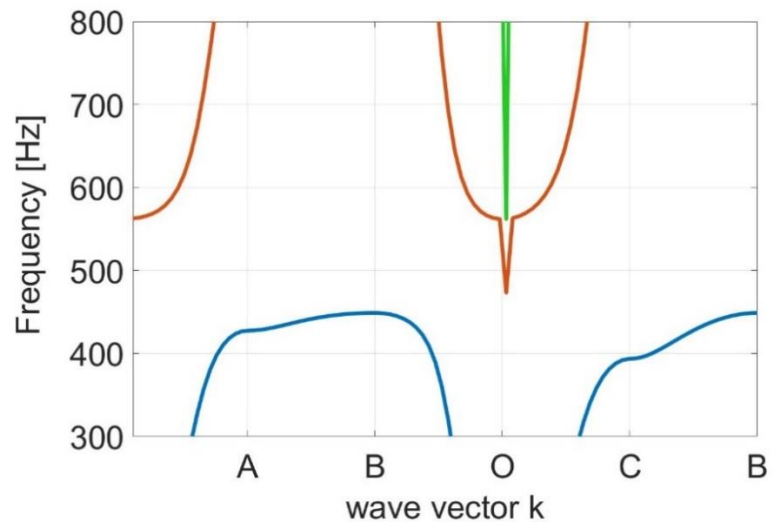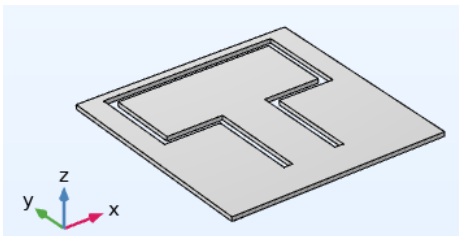
Figure 45: (left) unit cell design with a periodicity of 25 mm; (right) dispersion diagram for the 25 mm periodicity UC.

From the above dispersion diagrams a bandgap is found for the 443 – 517 Hz, 450– 537 Hz and 450 – 560 Hz frequency ranges for the 35 mm, 30 mm, 25 mm periodicity configurations respectively. For the bandgap evaluation in the 25 mm periodicity case it has been neglected the downward spike in the point O, that is probably due to an asymptote.
A trend can be noted in which the stopband is increased and shifted towards higher frequencies if the x and y periodicity is decreased.

6.3 T-element rescaling topology optimization

Now it is chosen to rescale the T-element into the 15 x 15 mm and 35 x 35 mm frames, instead of the original 20 x 20 mm dimensions. The considered Irreducible Brillouin Contour for the numerical simulations is the same as before and the obtained results are reported below.
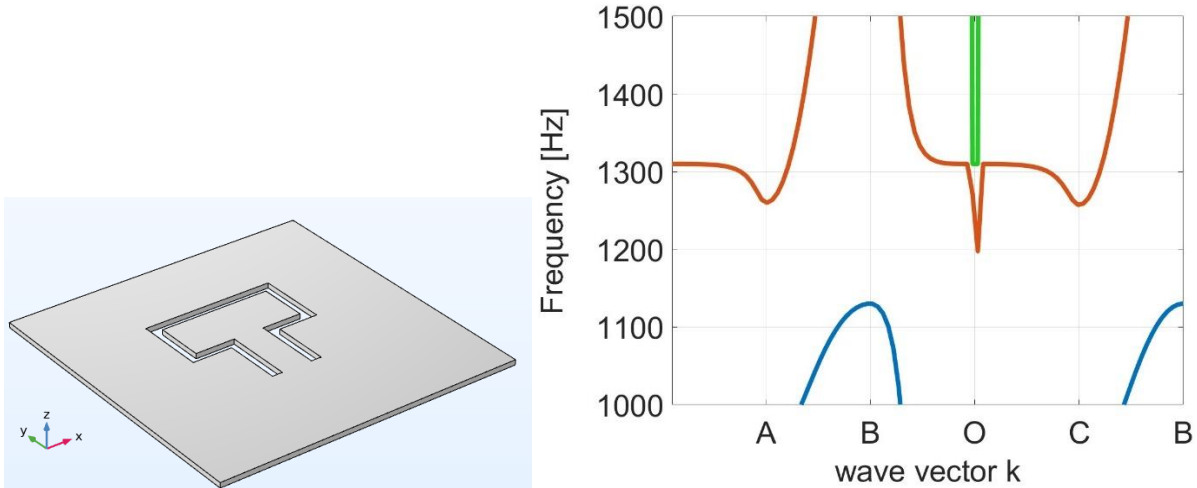
Figure 46: (left) unit cell design with a rescaled T element into the 15 x 15 mm frame; (right) dispersion curves relative to the unit cell.

In figure 46 is shown the tested unit cell, which is characterized by a 30 mm x and y axis periodicities. From the dispersion curves, instead, neglecting the downward spike in the point O, which is probably due to an asymptote, we can see a bandgap between 1130 and 1257 Hz, that is wider and rather shifted towards higher frequencies with respect to the original case study.
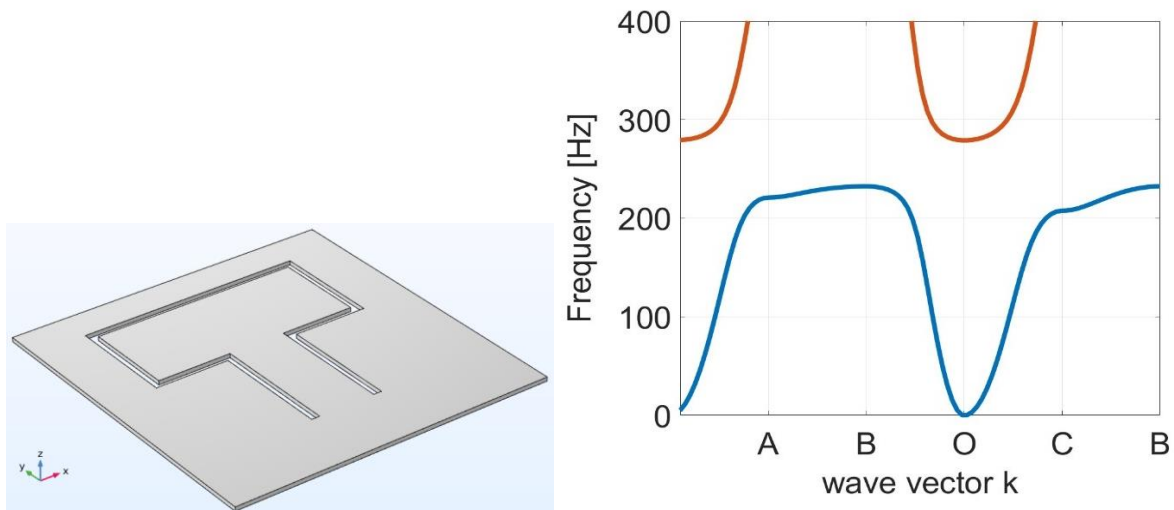
Figure 47: (left) unit cell design with a rescaled T element into the 35 x 35 mm frame; (right) dispersion curves relative to the unit cell.

In figure 47 is represented the 35 x 35 mm rescaled unit cell, whose periodicity is 40 mm.

From the obtained dispersion diagram above we can see that a stopband is found between 232Hz and 279 Hz. Compared to the original metamaterial configuration, the bandgap has moved towards lower frequencies, and it is less wide with respect to the precedent cases.

Then, basing on the previous results, a 20 mm x 20 mm frame with a 15 x 15 mm rescaled T-element is chosen. Knowing that a larger stopband is achieved if the periodicities is reduced and that it will be overly shifted towards higher frequencies (as shown in the precedent outcomes), it is decided to add a mass on the T shaped component, which has the effect to move towards lower frequencies the stopband.
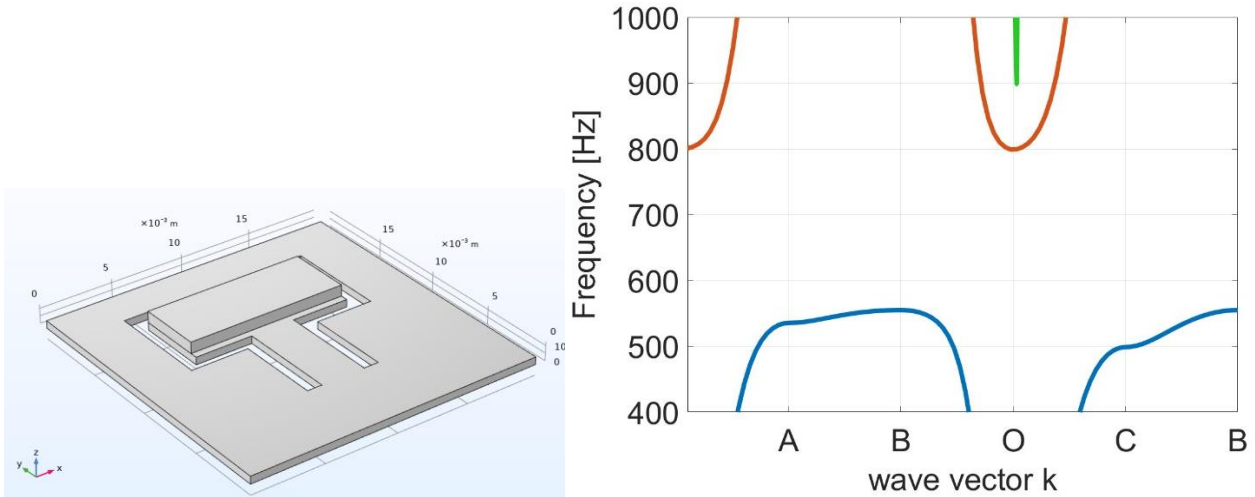
Figure 48: unit cell design with a rescaled T element into the 15 x 15 mm frame, a 20 mm periodicity and an added mass; (right) dispersion curves relative to the unit cell.

From the diagram in figure 48 it can be seen that the evaluated bandgap is between 555 Hz and 800 Hz. With this configuration it has been achieved a wider stopband in a more suitable frequency range, which is a really good accomplishment.

6.4 Material variation

Starting from the original unit cell configuration with a completely flat design and a 40 mm periodicity shown in figure 49, it has been varied the material from aluminium to steel.
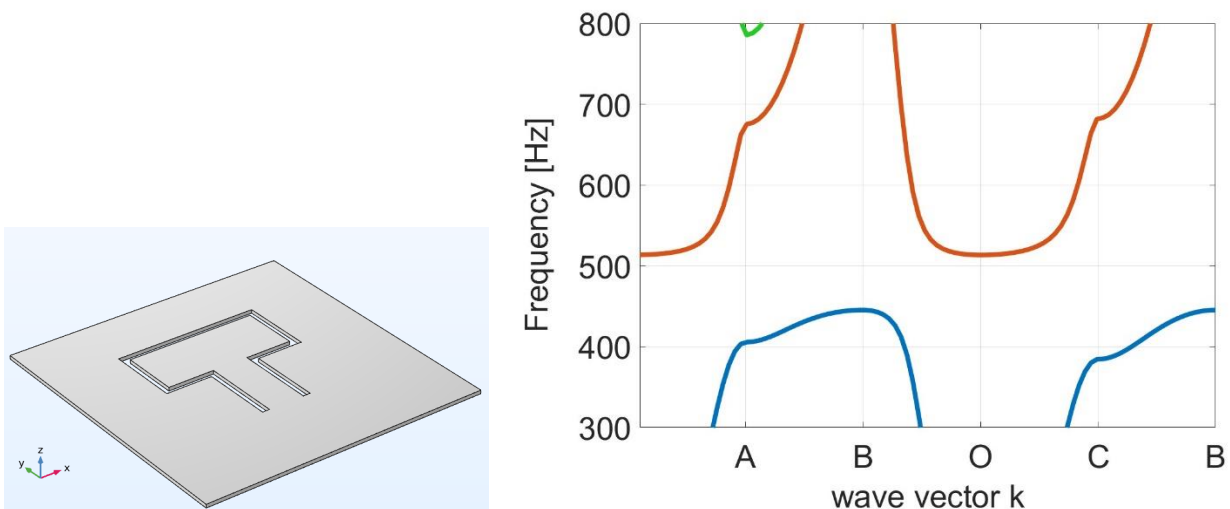
Figure 49: (left) steel unit cell design with a periodicity of 40 mm; (right) dispersion curves relative to the unit cell.

The obtained results in figure 49, show that a bandgap is found between 445 – 513 Hz. So, this unit cell concept has the same stopband width with respect to the original case, but it is slightly shifted towards higher frequencies.

6.5 Thickness variation

It is now considered the same unit cell configuration and material of the previous paragraph 6.4, with a change in the unit cell thickness from 0,5 mm to 1 mm, as represented in figure 50.
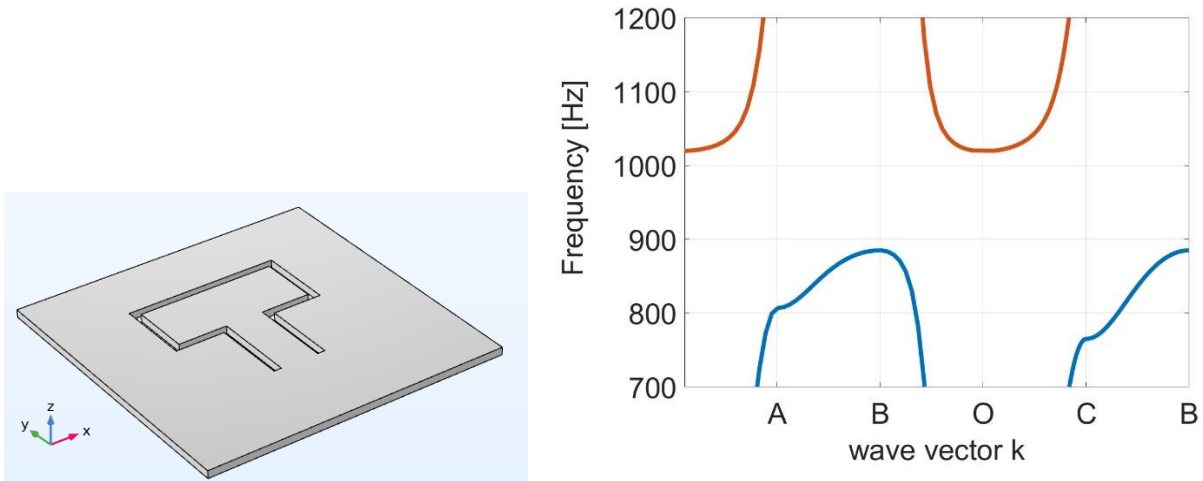
Figure 50: (left) steel unit cell design with a thickness of 1 mm; (right) dispersion curves relative to the unit cell.

From the simulation results reported in figure 50, a bandgap is noted in the 885-1020 Hz frequency range. Compared to the metamaterial configuration with half thickness, the bandgap has moved towards higher frequencies, and it is wider with respect to the precedent case.

Considering its performances and for ease of manufacturing, it has been chosen this unit cell design for the production of a metamaterial plate composed by 100 unit cells with a periodic distribution of 10 cells along both the x and y axis, as shown in figure 51.
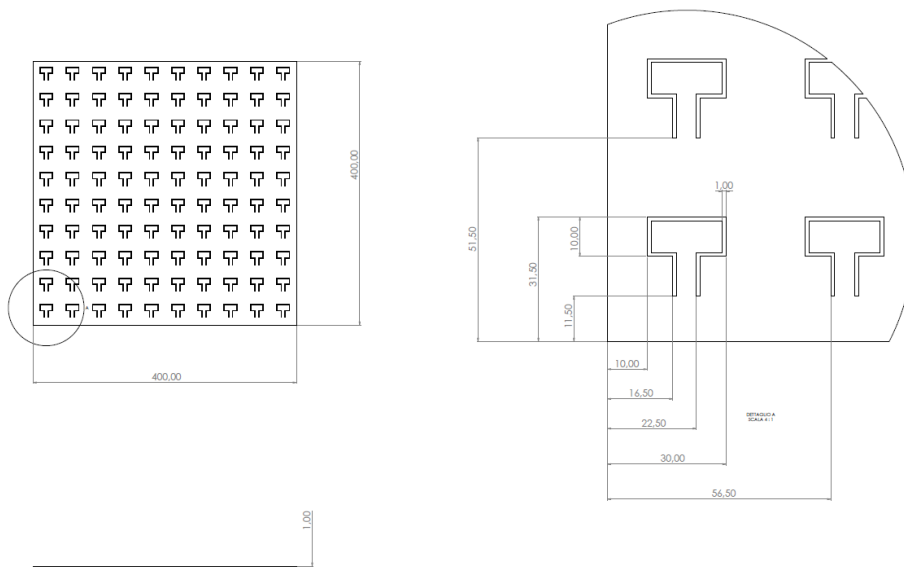
Figure 51: 2D drawing of the metamaterial plate for the production.

7. Summary tables

7.1 Literature review

7.1.1 Vibration applications, mechanical resonators

Resonator unit cell design	Resonator material	Bandgap [Hz]	Unit cell dimensions [mm]
Torsional local resonators	NA	87-90 (3)	NA
Z-shaped frame	aluminum	178-198 (20), 198-225 (27)	65 x 65
T-shaped	aluminum	615-635 (20)	40 x 40
Hollow parallelepiped	photopolymer	350-390 (40)	30 x 30
Composite sandwich with spiral resonators	SCFRPs and CCFRPs	490-600 (110)	20 x 25
Single cantilever beam	PMMA	490-540 (50)	25 x 25
Cantilever beam with endpoint mass	PMMA (body), steel (endpoint mass)	292 -323 (31)	35 x 20

7.1.2 Acoustic applications, mechanical resonators

Resonator unit cell design	Resonator material	Bandgap [Hz]	Unit cell dimensions [mm]
Basic spring-mass resonator	NA	445-644 (199)	50 x 50
Two cantilever beam	polyamide	193-224 (31)	65 x 25
Two separated beams	martensite-hardenable steel	227–243 (16), 243–273 (30)	36 x 36
Single-stage multi-DOF resonator	NA	370-390 (20), 455-465 (10), 810-850 (40)	30 x 30

Plate with multiple cantilever beams	NA	32- 37 (5)	300 x 75

7.1.3 Vibration applications, Helmholtz resonators

Resonator unit cell design	Resonator material	performances	Unit cell dimensions [mm]
Microperforated plate	aluminum	Two sound absorption peaks at 608 Hz and 926 Hz	60 x 60
SONOBEX Noise Trap panel	steel	60 dB transmission loss attenuation	200 x 200

7.2   Topology optimization

Unit cell design	Material	Periodicity [mm]	T element size [mm]	Thickness [mm]	Mass addition	Bandgap [Hz]
40/20	Aluminum	40	20	0.5	no	432-500 (68)
50/20	Aluminum	50	20	0.5	no	411-460 (49)
60/20	Aluminum	60	20	0.5	no	No complete bandgap
35/20	Aluminum	35	20	0.5	no	443-517 (74)
30/20	Aluminum	30	20	0.5	no	450-537 (87)
30/15	Aluminum	30	15	0.5	no	1130-1200 (70)
40/35	Aluminum	40	35	0.5	no	232-279 (47)
40/20	Steel	40	20	0.5	no	202-269 (67)
40/20	Aluminum	40	20	0.5	yes	443-513 (68)
40/20	Steel	40	20	1	no	885-1020 (135)

8. Conclusion

Initially, a literature review has been conducted in order to assess the state of the art about the metamaterial applications for the NVH field. Then, the T-shaped local resonator and the two cantilever beam metamaterials were chosen for the successive steps of the thesis, based on their attenuation performances and ease of manufacturing.

So, a numerical model has been developed for the evaluation of the dispersion curves using the COMSOL software. The obtained results, compared with the research paper ones, demonstrated the correctness of the numerical model.

Then, starting from the T-shaped local resonator solution reported in the paper, a different design has been proposed, characterized by a completely flat local resonator. A topology optimization has been performed, by varying the x and y axis unit cell periodicities and the scale of the T shaped element of the local resonator. Results showed that, when the periodicity was increased, a bandgap reduction took place. Instead, when the periodicity was decreased, a wider stopband has been noticed. The variation of the scale of the T element reduced the stopband width and influenced the region where the stopband was located: a smaller scale returned a bandgap shifted towards higher frequencies, while an increase in the scale led to a stopband transfer towards lower frequencies.

The change of the material unit cell from aluminium to steel did not influence the bandgap width, but it slightly shifted it towards higher frequencies. The addition of a small mass on the T shaped part of the local resonator generated a shifting of the bandgap towards lower frequencies, too.

By increasing the unit cell thickness, instead, it has been achieved a wider stopband that was also moved towards higher frequencies with respect to the original configuration.

Taking into account performances and manufacturing needs, it has been chosen the steel unit cell design with a 40 mm periodicity, a T-element size of 20 mm and a thickness equal to 1 mm for the production and the experimental validation phase of the thesis.

9. Acknowledgements

10. References

[1] L. Garibaldi and A. Daga, *Lesson 01 / A – Introduction and basis of NVH in vehicles,* 2021, Politecnico di Torino.

[2] M. Carello, NVH lessons, Politecnico di Torino, 2021.

[3] L. Y. L. Ang, Y. K. Koh and H. P. Lee, "Acoustic Metamaterials: A Potential for Cabin Noise Control in Automobiles and Armored Vehicles," *INTERNATIONAL JOURNAL OF APPLIED MECHANICS,* vol. 8, no. 5, 2016.

[4] M. Koichi and K. Yuhei, "3D printing of fiber composite sandwich metamaterial with spiral resonators for attenuation of low-frequency structural vibration," *Composites Part A: Applied Science and Manufacturing,* vol. 172, no. 107594, 2023.

[5] I. Raza and H. Mohammad, "Additive manufacturing of locally resonant metamaterials," Imperial College London, 2017, doi: https://doi.org/10.25560/54773.

[6] J. Yupei, H. Guobiao, T. Lihua and C. A. Kean, "Band Gap Formation in Metamaterial Beam With Torsional Local Resonators for Vibration Suppression.," in *Proceedings of the ASME 2020 Conference on Smart Materials, Adaptive Structures and Intelligent Systems. ASME 2020 Conference on Smart Materials, Adaptive Structures and Intelligent Systems*, 2020.

[7] S. Riess et al., "Vibroacoustic Metamaterials for enhanced acoustic Behavior of Vehicle Doors," in *Fifteenth International Congress on Artificial Materials for Novel Wave Phenomena (Metamaterials)*, 2021, NYC, NY, USA, 2021, pp. 374-376, doi: 10.1109/Metamaterials52332.2021.9577065.

[8] L. Brillouin, Wave Propagation in Periodic Structures 2nd, McGraw-Hill Book Company, 1946.

[9] A. Melnikov, M. Hanke and S. Marburg, "Dispersion Curves of Elastic Metamaterials and Sonic Crystals with ANSYS," 2018, CASCON Conference, Leipzig.

[10] R. Langley, "A Note On The Force Boundary Conditions For Two-Dimensional Periodic Structures With Corner Freedoms," *Journal of Sound and Vibration,* vol. 167, no. 2, pp. 377-381, 1993, ISSN 0022-460X, https://doi.org/10.1006/jsvi.1993.1341.

[11] L. Van Belle and W. Desmet, "Damping in a locally resonant metamaterial using inverse and direct unit cell modelling," in *11th International Congress on Engineered Materials Platforms for Novel Wave Phenomena (Metamaterials)*, Marseille, France, 2017.

[12] E. Groth, I. Iturrioz and T. Clarke, "The dispersion curve applied in guided wave propagation in prismatic rods," *Latin American Journal of Solids and Structures,* vol. 15, no. 6, 2018, 1590/1679-78254527, doi:10.1590/1679-78254527.

[13] M. Yuxuan, C. Lihua, Z. Mengjiao and Z. Yadi, "A Local Resonance Metamaterial For Vibration Reduction," in *2021 4th World Conference on Mechanical Engineering and Intelligent Manufacturing (WCMEIM)*, Shanghai, China, 12-14 November 2021.

[14] C. Nerse, R. Schadeberg and S. Oberst, "Novel resonator geometry for easily manufactured tunable locally resonant metamaterial," in *2021 Annual Conference of the Australian Acoustical Society 2021: Making Waves, AAS 2021*, Woolongong, 2021.

[15] N. F. Melo, C. Claeys, E. Deckers, B. Pluymers and W. Desmet, "Dynamic Metamaterials for Structural Stopband Creation," in *SAE Int. J. Passeng. Cars - Mech. Syst., 9th International Styrian Noise, Vibration & Harshness Congress: The European Automotive Noise Conference, 9(3):1013-1019, 2016, https://doi.org/10.4271/2016-01-1791*.

[16] L. Sangiuliano, C. Claeys, E. Deckers, B. Pluymers and W. Desmet, "Force Isolation by Locally Resonant Metamaterials to Reduce NVH," SAE, 2018.

[17] Z. Honggang, Z. Qiquan, W. Yang, C. Junhui, W. Chao and W. Jihong, "Acoustic absorption of a metamaterial panel: Mechanism, boundary effect and experimental demonstration," *Applied Acoustics,* vol. 184, 2021, 108369, ISSN 0003-682X, https://doi.org/10.1016/j.apacoust.2021.108369.

[18] K. Dev and U. Priyank, "Design and optimization of acoustic sound absorbers for low frequency sounds," in *AIP Conference Proceedings*, 5 May 2023, 2584 (1): 020011, https://doi.org/10.1063/5.0128063.

[19] L. Van Belle, C. Claeys, E. Deckers and W. Desmet, "Sound Transmission Loss of Locally Resonant Metamaterial and Phononic Crystal Plates," in *12th International Congress on Artificial Materials for Novel Wave Phenomena (Metamaterials), Espoo, Finland, 2018, pp. 413-415, doi: 10.1109/MetaMaterials.2018.8534069*, 2018.

[20] L. Sangiuliano, C. Claeys, E. Deckers, J. De Smet, B. Pluymers and W. Desmet, "Reducing Vehicle Interior NVH by Means of Locally Resonant Metamaterial Patches on Rear Shock Towers," in *SAE Technical Paper 2019-01-1502*, 2019, https://doi.org/10.4271/2019-01-1502.

[21] L. Sangiuliano, B. Reff, J. Palandri, F. Wolf-Monheim, B. Pluymers, E. Deckers, W. Desmet and C. Claeys, "Low frequency tyre noise mitigation in a vehicle using metal 3D printed resonant metamaterials," *MECHANICAL SYSTEMS AND SIGNAL PROCESSING,* vol. 179, no. 109335, 2022, DOI: 10.1016/j.ymssp.2022.109335.

[22] Z. Gong, X. Meng, W. Xiao and W. Ting, "Low-frequency vibroacoustic performance of an acoustic metamaterial plate with periodical single-stage multi-degree-of-freedom resonators attachment," *Physics Letters A,* vol. 412, 2021, 127593, ISSN 0375-9601, https://doi.org/10.1016/j.physleta.2021.127593.

[23] Y. Liao, H. Huang, G. Chang, D. Luo, C. Xu, Y. Wu and J. Tang, "Research on Low-Frequency Noise Control of Automobiles Based on Acoustic Metamaterial," *Materials (Basel),* 2022 May 1, 15(9):3261, doi: 10.3390/ma15093261.

[24] C. Hakoda, J. Rose, P. Shokouhi and C. Lissenden, "Using Floquet periodicity to easily calculate dispersion curves and wave structures of homogeneous waveguides," *AIP Conf. Proc. ,* 20 April 2018 1949 (1): 020016. https://doi.org/10.1063/1.5031513.